UNIVERSITA' DELLA BASILICATA
POTENZA

DIPARTIMENTO
DI
INGEGNERIA E FISICA DELL'AMBIENTE

DOTTORATO DI RICERCA
IN
INGEGNERIA DELL'AMBIENTE
XXI CICLO

Synthetic Aperture Radar Interferometry Advances for the Analysis of Deformation Phenomena related to Subsidence and Hydrogeological Instability

GIOVANNI ZENI

UNIVERSITA' DELLA BASILICATA
POTENZA

DIPARTIMENTO
DI
INGEGNERIA E FISICA DELL'AMBIENTE

DOTTORATO DI RICERCA
IN
INGEGNERIA DELL'AMBIENTE
XXI CICLO
(FIS/06)

Synthetic Aperture Radar Interferometry Advances for the Analysis of Deformation Phenomena related to Subsidence and Hydrogeological Instability

Coordinatore:

Prof. Gian Lorenzo Valenti

Tutor:
Prof. Carmine SERIO

Dottorando:
Giovanni ZENI

Co-Tutor:
Ing. Riccardo LANARI

Table of contents

Abstract

The use of advanced satellite techniques, such as those involving data achieved by space-borne Synthetic Aperture Radar (SAR), can be extremely useful and complement with conventional methods in the analysis of subsidence and slow-moving landslide phenomena.

These are widespread all over the world where systematically cause significant damage to structure/infrastructures.

Synthetic Aperture Radar (SAR) is a coherent active microwave remote sensing system, able to perform accurate distance measurements between the sensor platform and the target on the ground. The SAR interferometry is based, in its first application, on the exploitation of two different SAR images to extract the corresponding phase difference, which is related to the topography of the illuminated scene. Within the SAR technology, an important improvement has been gained with the introduction of the differential SAR interferometry (DInSAR). DInSAR methodology allows to isolate the contribution due to the deformation of the scene occurred between the two flights of the radar sensor.

The advanced DInSAR technique referred to as Small BAseline Subset (SBAS) approach, with a particular emphasis on the applications in the subsidence phenomena, ground deformation and landslide monitoring, will be the key point of this work.

In particular, following a brief introduction concerning the basic principles of the SAR image formation, the InSAR technologies for the estimation of the scene topography will be presented and the main limitations of the DInSAR techniques will be analyzed.

Subsequently, the extension of the DInSAR methodology to analyze the temporal evolution of the deformation, which are evaluated by exploiting a whole set of multiple differential interferograms will be provided. Finally an overview on the basic rationale of the applied two-scale SBAS approach is presented.

The general features of subsidence and slow-moving landslide phenomena and the application of the SBAS-DInSAR approach to real cases by using several independent SAR data-set will be exploited.

The first one focuses on a DInSAR survey carried out on an area of about 400 Km^2 in Basilicata region, Italy, that allows to detect a

ground deformation effect involving the urban area of Satriano di Lucania, located close to Potenza, and to analyze the Maratea Valley deformation phenomena.

Subsequently the two scale SBAS technique is used to investigate subsidence phenomena and, thus, to provide useful information for the detection of building damage susceptibility in the Sarno town and in the city of Rome (Italy). Finally, ground deformation analysis affecting the Umbria region (central Italy) is presented. In particular, it is aimed to identify and measure subsidence phenomena induced by exploitation of a confined aquifer in the Valle Umbra, to monitor and measure the landslides and landslide areas percentage, and to investigate the movement of the Ivancich landslide, in the Assisi Municipality.

A discussion, concerning the achieved results and the future improvement of the exploited DInSAR techniques, will conclude the present work.

This PhD Thesis represents one of the first examples of extensive use of DInSAR technology devoted to the subsidence phenomena and hydrogeological instability analysis.

Introduction

Subsidence and slow-moving landslide phenomena are widespread all over the world where systematically cause significant damage to structure/infrastructures. In the field of land use and management, several scientific works dealing with: the analysis of predisposing factors and triggering causes; the investigation of the evolution mechanisms; the development of in-situ surveys and laboratory tests are present. These studies, to be useful, need a huge number of displacement measurements, in space and time, that can turn out to be expensive and time-consuming if carried out, especially over large areas, via conventional monitoring techniques.

With this regard, the use of advanced satellite techniques, such as those involving data achieved by space-borne Synthetic Aperture Radar (SAR), can be extremely useful and can complement with conventional methods due to the achieved large area coverage and the availability of image archives covering more than a decade.

SAR is a coherent active microwave remote sensing system, able to perform accurate distance measurements between the sensor platform and the target on the ground. Within the SAR technology, an important improvement has been gained with the introduction of the interferometric SAR (InSAR) technique. It is based, in its basic form, on the exploitation of two different SAR images to extract the corresponding phase difference, which is related to the topography of the illuminated scene and to the acquisition orbit separation (baseline).

A further improvement has been realized when the differential SAR interferometry (DInSAR) has been introduced. DInSAR methodology allows to simulate the topography phase screen and to isolate the contribution due to the deformation of the scene occurred between the two flights of the radar sensor.

The advance on the DInSAR technology, and the technique referred to as Small BAseline Subset (SBAS) approach, with a particular emphasis on the applications in the subsidence phenomena, ground deformation and landslide monitoring, will be the key point of this work, which is organized as follows:

- Chapter I - After a brief introduction concerning the basic principles of the SAR image formation, the InSAR

technologies for the estimation of the scene topography will be presented. Finally, the Differential InSAR technique and its main limitations will be analyzed.

- Chapter II – The topic of this chapter will concern the discussion of the extension of the DInSAR methodology to analyze the temporal evolution of the deformation which are evaluated by exploiting a whole set of multiple differential interferograms. An overview on the basic rationale of the applied two-scale SBAS approach, will also be presented .
- Chapter III - This chapter deals with the general features of subsidence and slow-moving landslide phenomena and the application of the formerly presented DInSAR approach to real cases. For this purpose, several independent SAR data-set will be used and the achieved results will be analyzed.
- Chapter IV - This chapter focuses on the DInSAR survey carried out on an area of about 400 Km^2 in Basilicata region, Italy, that allows to detect a ground deformation effect involving the urban area of Satriano di Lucania, located close to Potenza, and to analyze the Maratea Valley deformation phenomena, as well.
- Chapter V - In this chapter the two scale SBAS technique is used to investigate subsidence phenomena and, thus, to provide useful information for the detection of building damage susceptibility in the Sarno town (Italy).
- Chapter VI - This chapter will address the analysis of the surface deformation at two distinct spatial scales: a low resolution, large scale, and a fine resolution, local scale on the city of Rome (Italy).
- Chapter VII - In this chapter the analysis of ground deformation affecting the Umbria region (central Italy) is presented. In particular, it is aimed to identify subsidence phenomena induced by exploitation of a confined aquifer in the Valle Umbra; to monitor and measure the landslides and landslide areas percentage using DInSAR technique, and to investigate the displacements of the Ivancich landslide, in the Assisi Municipality.

A discussion, concerning the achieved results and the future improvement of the exploited DInSAR techniques, will conclude the present work.

Chapter 1

SAR Interferometry

1.1 Introduction

Synthetic Aperture Radar (SAR) is a coherent active microwave remote sensing system, whose capability to effectively map the scattering properties of the Earth's surface has been already intensively investigated.

A SAR sensor, which can be mounted on-board to an aircraft and/or a satellite, has a side-looking illumination direction and is able to perform accurate distance measurements between the moving platform and the surface. Both the acquisition geometry and the physical characteristics of the scene contribute to the formation of the received backscattered radar signal (echo) which, properly processed, leads to the reconstruction of a complex high resolution SAR image. Moreover, being an active imaging sensor, it does not need an external energy source to work and, exploiting the microwave region of the electromagnetic spectrum, can be effectively used to detect areas affected by a significant clouds' cover. As a consequence of its flexibility, SAR technology mostly improved during the last years and further techniques have been also developed, thus helping the scientific community on the interpretation of several geophysical phenomena.

One of the major applications of the SAR technology is represented by the SAR Interferometry (InSAR) technique which exploits, in its basic form, the phase difference of (at least) two complex-valued SAR images (acquired from different orbit positions and at different times) to measure several quantities, such as topography, deformation, etc…

This work will be focused on the study of Advanced InSAR techniques with a particular emphasis on the applications in the subsidence phenomena, ground deformation and landslide monitoring
This chapter, in particular, will address the key topics of the SAR technology, with a particular emphasis on the InSAR applications.

1.2 SAR History

Since the 1950's when Carl Wiley [1] made his first observations about the "Doppler beam-sharpening" phenomenon, SAR designs and related applications have grown exponentially.
In 1974 an agreement between JPL (Jet Propulsion Laboratory) engineers with a group of international ocean scientists led the National Oceanic and Atmospheric Administration (NOAA) to determine if an ocean application satellite, featuring a space-based SAR, could be achieved. Their efforts were directed to the realization of a satellite SAR system, which was launched in 1978 onboard to the SEASAT [2] sensor,

The 1990's witnessed a significant expansion of SAR missions with the launch of five Earth-oriented SAR satellites. The NASA continued with the Space Shuttle Imaging Radar SAR mission in 1994. Nevertheless, the real breakthrough in SAR Interferometry has been achieved by the twin European ERS-1/2 (European Remote Sensing Satellite) sensors [3], launched in 1991 and 1995, respectively, which, with respect to the stability, calibration, etc., represent nowadays the best goal achieved with SAR in the Interferometry area.

Also Japan and Canada launched a SAR system in 1992 (JERS) and in 1995 (Radarsat), respectively, but various problems limited the exploitation of these sensors.

In practice, for more than a decade SAR images from space have been available on a reliable routine basis for scientific, public, and commercial users, independent of weather and daylight conditions. The most successful SAR workhorses have been ERS-1/2, and, since March 2002, ENVISAT [11]. Generation of digital elevation models (DEMs), measurement of glacier flows, and mapping of earthquakes, volcanoes and subsidence are the most

prominent fields of interest today. The majority of interferometric applications today use data of ERS-1/2 and RADARSAT (both C-band SARs) while the only source of L-band data was the late Japanese JERS. [4] Besides, a new generation of SAR satellites is now available: the German SARLupe and TerraSAR-X, the Canadian Radarsat-2, the Italian COSMO-Skymed and the Japanese Advanced Land Observing Satellite (ALOS) [5]. In this context, a key role could be played in the future, in particular, by the ALOS-PALSAR system (launched in January, 24th 2006), which is working at L-band.

1.3 SAR Sensors and Images Characteristic

A SAR imaging geometry from a satellite (such as ERS or Envisat) is sketched in Figure 1. A satellite carries a radar with the antenna pointed to the Earth's surface in the plane perpendicular to the orbit. The inclination of the antenna with respect to the nadir is called the off-nadir angle and in contemporary systems is usually in the range between 20° and 50° (it is 21° for ERS). Due to the curvature of the Earth's surface, the incidence angle of the radiation on a flat horizontal terrain is larger than the off-nadir (typically 23° for ERS). However, for the sake of simplicity it is assumed here that the Earth is flat, and hence that the incidence angle is equal to the off-nadir angle, as shown in the figure.

Currently, operational satellite SAR systems work in one of the

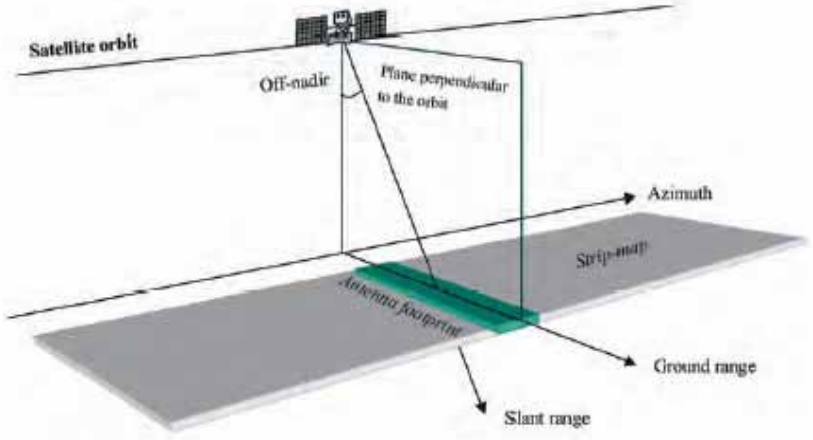

Figure 1. 1

A space-based SAR system

following microwave bands:
• C band – 5.3 GHz (ESA's ERS and Envisat, the Canadian Radarsat, and the US shuttle missions)
• L band – 1.2 GHz (the Japanese J-ERS and ALOS)
• X band – 9.6 GHz (the German-Italian X-SAR on the shuttle missions)

In the case of ERS, the illuminated area on the ground (the antenna footprint) is about 5 km in the along-track direction (also called the azimuth direction) and about 100 km in the across-track direction (also called the ground range direction). The direction along the Line of Sight (LOS) sensor-target is usually called the slant-range direction. The footprint, due to platform motion, traces a swath 100 km wide in ground range on the Earth's surface, with the capability of imaging a strip 445 km long every minute (strip map mode).

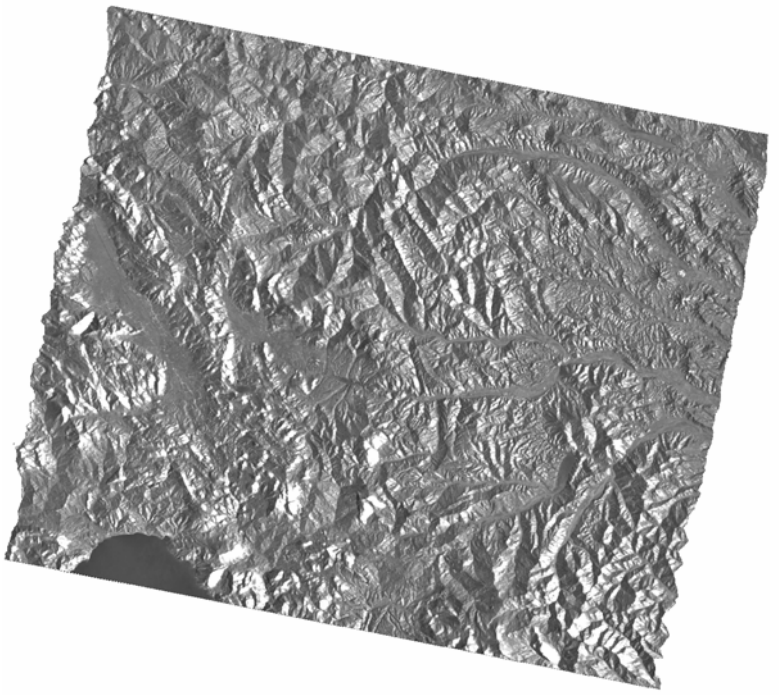

Figure 1. 2

An example of multilook SAR image of the Basilicata region (Southern Italy)

A digital SAR image can be seen as a mosaic (i.e. a two-dimensional array formed by columns and rows) of small picture elements (pixels). Each pixel is associated with a small area of the Earth's surface (called a resolution cell). More precisely, the resolution (depending on the sensor characteristics) is smaller then the pixel dimension (depending on the sampling of the received signals); however, for our analysis were simplify the discussion by assuming the equivalence between resolution cell and pixel dimension. Each pixel gives a complex number that carries amplitude and phase information about the microwave field backscattered by all the scatterers (rocks, vegetation, buildings etc.) within the corresponding resolution cell projected on the ground. Different rows of the image are associated with different azimuth locations, whereas different columns indicate different slant range locations.

In the ERS case, the SAR resolution cell dimension is about 5 metres in azimuth and about 9.5 metres in slant-range. The SAR resolution cells are thus slightly overlapped both in azimuth and in slant-range.

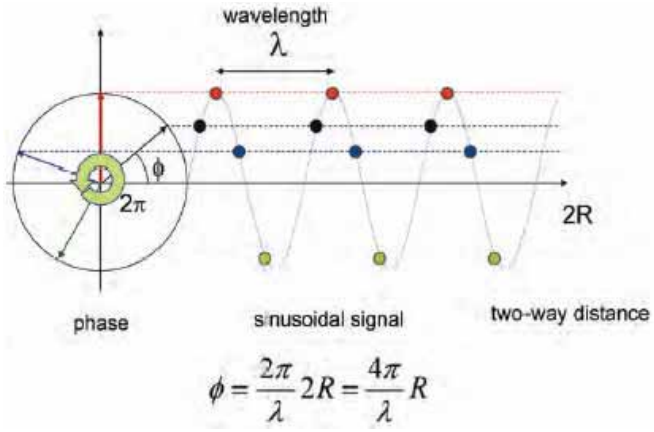

Figure 1. 3

A sinusoidal function sin φ is periodic with a 2 π radian period. In the case of a relative narrow-band SAR (i.e. ERS and Envisat), the transmitted signal can be assimilated, as a first approximation, to a pure sinusoid whose angle or phase φ has the following linear dependence on the slant range coordinate r: φ = 2 πr /λ (where λ is the SAR wavelength). Thus, assuming that the phase of the transmitted signal is zero, the received signal that covers the distance 2R travelling from the satellite to the target and back, shows a phase φ = 4 πR/ λ radians

The detected SAR image contains a measurement of the amplitude of the radiation backscattered toward the radar by the objects (scatterers) contained in each SAR resolution cell. This amplitude depends more on the roughness than on the chemical composition of the scatterers on the terrain. Typically, exposed rocks and urban areas show strong amplitudes, whereas smooth flat surfaces (like quiet water basins) show low amplitudes, since the radiation is mainly mirrored away from the radar. The detected SAR image is generally visualised by means of grey scale levels as shown in the example of Figure 1.2. Bright pixels correspond to areas of strong backscattered radiation (e.g. urban areas), whereas dark pixels correspond to low backscattered radiation (e.g. a quiet water basin).

The radiation transmitted from the radar has to reach the scatterers on the ground and then come back to the radar in order to form the SAR image (two-way travel). Scatterers at different distances from the radar (different slant ranges) introduce different delays between transmission and reception of the radiation.

In real scenarios the SAR sensors transmit appropriate signals (modulated pulses); however, in order to simplify the discussion loosing the rationale of the analysis, we assume to transmit purely sinusoidal signals. The above mentioned sensor target distance introduces delay τ which is equivalent to a phase change $\Delta\phi$ between transmitted and received signals. The phase change is thus proportional to the two-way travel distance 2R of the radiation divided by the transmitted wavelength λ. This concept is illustrated in Figure 1.3. However, due to the periodic nature of the signal, travel distances that differ by an integer multiple of the wavelength introduce exactly the same phase change. In other words, the phase of the SAR signal is a measure of just the last fraction of the two-way travel distance that is smaller than the transmitted wavelength.

By measuring the phase difference between the echoes of the same target in two different times (repeat observations), the SAR system may achieve information about possible variations of the range distance and, therefore, of possible displacements of the target under investigation.

This is the key principle in differential Interferometry that exploit the phase difference of temporarly separated complex SAR images. Obviously, even in such an ideal noise/disturbance free case

the measure is inherently restricted in 2π interval and thus unwrapping problems must be faced.

Interferometry, including the analysis of decorrelation and atmospheric contribution are the subject of the next section. Hereafter, the problems related to geometric distortions induced by the slant imaging geometry are discussed.

The terrain area imaged in each SAR resolution cell (called the

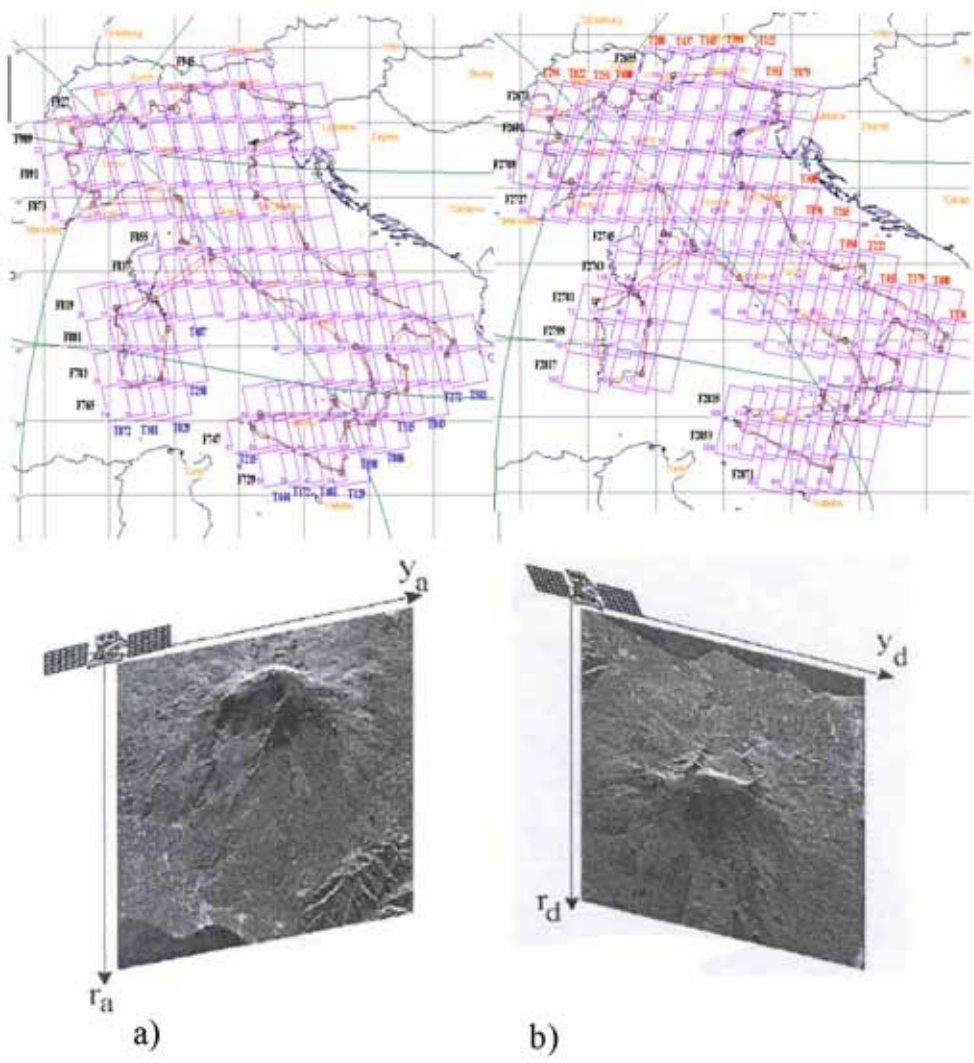

Figure 1. 4

Full coverage and image of Etna Volcano (Sicily, Italy) taken from:
a) ascending and b) descending passes

ground resolution cell) depends on the local topography. It strongly depends on the terrain slope in the plane perpendicular to the orbit (ground range direction) and on the terrain slope in the azimuth direction. The dimension of the ground resolution cell in azimuth is related to that of the SAR resolution cell by the usual perspective deformation experienced when looking at surfaces from a non-nadir direction.

ERS sensors offer the possibility to observe the same scene with incidence angles of both plus and minus 23 degrees. This is due to the fact that during orbits that go from South to North (ascending passes) and from North to South (descending passes), the SAR antenna pointing is usually fixed to the same side of the orbital plane with respect to the velocity vector (e.g. the radar antenna is always pointed to the right side of the track for ERS and Envisat). Thus, the same scene on the ground is observed by the SAR antenna from the east during the descending passes and from the west during the ascending passes.

In Figure 1.4 a-b two detected ERS images of Mount Etna (Italy) taken from ascending and descending passes are shown together with full coverage of Italian territory by ERS passes. A comparison of these two images clearly shows the effect of the different perspective: the summit is shifted away from the coastline in the ascending (left) ERS SAR image and towards it in the descending (right) image. From these images it is also evident that high resolution details of the western flank of the volcano are obtained from ERS ascending passes, whereas the eastern flank is ‘squeezed’ into a few pixels of the SAR image (usually referred to “layover effect”); the opposite happens with descending ERS passes. Thus, both ascending and descending passes should be exploited to get a high resolution SAR image of the whole area.

1.4 Basics and Limitations of SAR Interferometry

The basic principle of interferometry relies on the fact that the phase of SAR images is an ambiguous (modulo- 2π) measure of the sensor-target distance. Therefore, distance variations can be determined by computing, on a pixel by pixel basis, the phase difference (interferometric phase) relative to two SAR images (standard two-pass interferometry). This is actually performed as pixel by pixel product of the reference image (**master**) times the complex conjugated secondary (**slave**) image (Figure 1.5). As already mentioned, each SAR image pixel represents the coherent sum of all scattering elements within a resolution cell.
Moreover, each element contributes both with its own complex

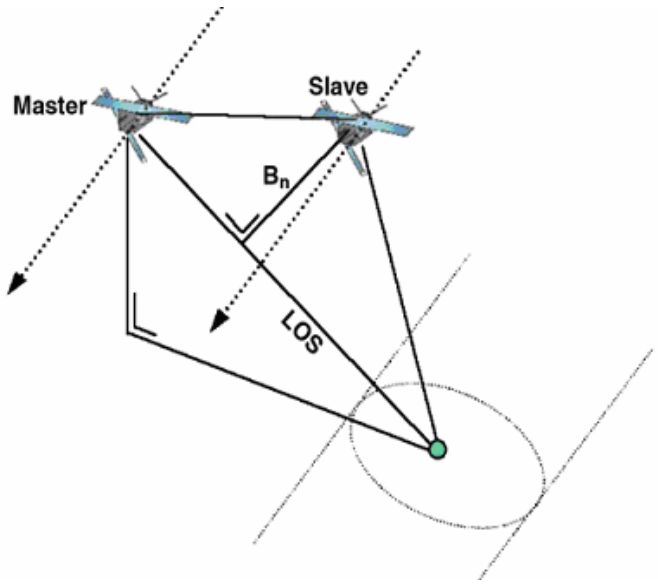

Figure 1. 5

Simplified geometry of interferometric measurements

reflectivity (amplitude and phase) and with its individual distance from the sensor.

The coherent image formation mechanism coupled with the high phase sensitivity prevents the phase value relative to an individual pixel of a single SAR image from being directly exploitable. On the other hand, as long as the complex reflectivity of the pixel as a whole (i.e. the reflectivity of the elementary scatterers and their differential sensor-target path) does not change in the time span between successive radar acquisitions, it is cancelled out from the interferometric phase, thus allowing the measurement of the variation of the range path to the scatterers within the resolution cell. This is the basic assumption for carrying out interferometric measurements and is referred to as absence of decorrelation (or full **coherence**).

In reality, a residual differential reflectivity term always affects the interferometric phase and is referred to as decorrelation noise. In particular, vegetated areas are often afflicted by **temporal decorrelation** because of a complex reflectivity varying with time and/or position of the elementary scatterers within the sampling cell (e.g. leaves and small branches of a tree).

Conversely, **geometric decorrelation** is due to a complex reflectivity that changes with the acquisition geometry [6]. Geometric decorrelation is mainly due to the presence of plural comparable (in terms of the backscattered radiation) scatterers within a single sampling cell. Their differential travel path varies with the acquisition geometry. The key orbital parameter controlling this effect is the so-called **normal baseline b**, i.e. the projection perpendicular to the line-of-sight (LOS) direction of the distance of the satellite orbits relative to the two images involved in the interferogram (Figure 1.5)

Briefly, the **interferometric phase** is the combination of several terms that can be classified in two main categories:

- geometric (**deterministic**) terms associated to the target-to-radar path difference;
- **stochastic** phase shift (noise) terms.

Mathematically, the phase difference Δφ, related to a generic pixel can be expressed as follows:

$$\Delta\phi = \Delta\phi_{geo} + \Delta n \qquad (1.1)$$

wherein, $\Delta\phi_{geo}$ is the geometric term and Δn the stochastic one.

Geometric terms are induced by the target topography in association with the presence of an angular view difference due to the spatial baseline, and a possible target displacement occurring between the passes (Figure 1.6):

$$\Delta\phi = \Delta\phi_{geo} = \Delta\phi^{topo} + \frac{4\pi}{\lambda} d \qquad (1.2)$$

with λ the transmitted signal wavelength equal to 5.6 cm for sensor operating at C-band (ERS, Envisat, etc.).
With reference to the first term in (1.2), the interferometric sensitivity to topography is much lower and is proportional to the normal baseline of the interferogram at hand (the normal baseline is a measure of how different the two orbits are); it can be written as:

$$\Delta\phi^{topo_{1,2}} = \frac{4\pi}{\lambda r_1 \sin\theta} B_n$$

where $\Delta\phi^{topo1,2}$ is the topographic contribution to the interferometric phase difference between two arbitrary pixels (named 1 and 2), $d(t_n)$ is the sensor-target distance (approximately 845 km for ERS mid-range), is $B_n = B\left[\cos(\theta - \alpha)\right]$ where Bn is the perpendicular component of the spatial separation brtween orbits (B, referred to baseline); z is the topographic height difference of the two scatterers in the two pixels and θ is the incidence angle with respect to the "flat earth".

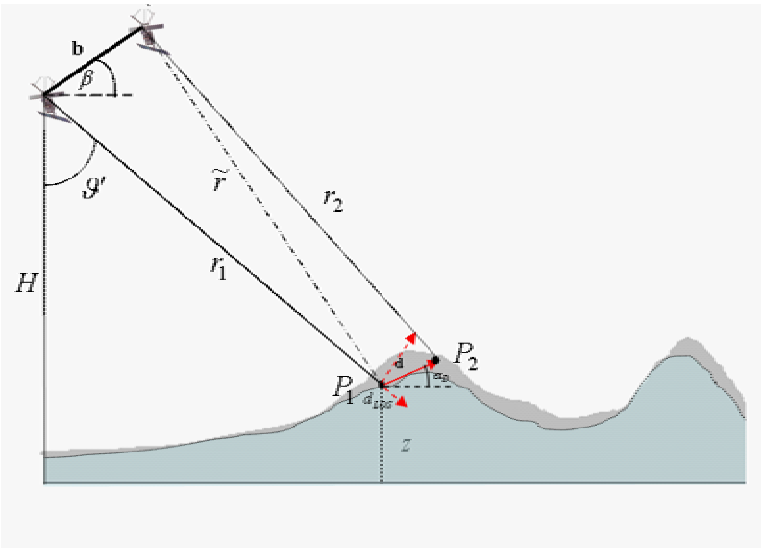

Figure 1. 6

Acquisition geometry

The topographic sensitivity of an interferogram is usually quantified by the height of ambiguity [7] [8] , i.e. the relative height difference $h_{2\pi}$ between two image pixels that introduces a full phase cycle:

$$h_{2\pi} = \frac{\lambda r_1 \sin\theta}{2B_n} \approx (\,for ERS) 9350 / B_n \ \text{[m]}$$

Referring to equation (1.2), the second term corresponds to the possible ground deformation d affecting directly the sensor-target travel path, since SAR systems appreciate only the LOS projection (Δs_{LOS}) of the occurring deformation:

$$\Delta\phi_{def,LOS} = (4\pi / \lambda) d$$

The sensitivity is very high: a LOS displacement of λ/2 causes a full phase cycle; λ is on the order of centimetres at microwaves.

The **Stochastic contributions** in equation (1.1) are due to:

- changes of the scattering properties due to temporal modification (**temporal decorrelation**) and/or to the different interaction mechanisms between the electromagnetic wave and the ground surface associated to the angular view difference (**spatial decorrelation).**
- propagation delay variation due to the presence of the atmosphere (Atmospheric Phase Screen, or briefly APS).
  Although SAR systems are capable of penetrating the cloud cover, the SAR phase signal is significantly influenced by the atmospheric conditions, in particular by the water vapour distribution in the troposphere [9] [10]. The atmospheric phase distortion (atmospheric phase screen, APS) is strongly correlated in space within each individual SAR image (i.e. it varies smoothly as a function of range and azimuth).
- receiver noise contributions (**thermal noise decorrelation**).
- **processing artifacts and orbital information inaccuracies**.

These latter (in particular baseline errors) translate into a further spatially correlated phase term (a low order phase polynomial).

The **stochastic terms** can be expressed as follows:

$$\Delta n = \Delta n\_low + \Delta n\_high \qquad (1.3)$$

wherein Δn_low is mainly associated with the APS and to the orbital errors and Δn_high to the decorrelation effects, the thermal noise and processing artefacts. The former is a spatially correlated and temporally uncorrelated contribution and, as consequence, can be reliably estimated only by using a set of interferograms, rather than a single acquisition pair, as better explained in the following.

Accordingly, if stochastic contributions are “low”, or “kept low” via averages or ad-hoc filtering procedures, by knowing the target height from an external Digital Elevation Model (DEM), the topography contribution can be subtracted from the interferogram (differential interferogram generation) thus accessing to the deformation measure.

Indeed, after topography removal, the differential phase $\Delta\phi$ can be written as follows:

$$\Delta\phi = 2\pi \frac{\Delta z}{h_{2\pi}} + \frac{4\pi}{\lambda} d + \Delta n \qquad (1.4)$$

wherein Δz is the possible topography error associated with the external DEM.

Thus, if Δz and Δn are low or properly mitigated, the target displacement, or better, its component along the LOS can be reliably measured with an accuracy of the order of the radar wavelength (5.6 cm for the C-Band radar systems mounted onboard the ERS and Envisat satellites of the European Space Agency).

Processing artifacts can be limited by using accurate algorithms for focusing and, particularly for the alignment (registration) of the two images before compare the phase difference.

Orbital information inaccuracies can be controlled because they appear as low order spatial contributions on images covering 80x80 km, such as those associated to a frame of ERS and Envisat-ASAR (ERS-like mode) data.

Thermal noise decorrelation is generally negligible, unless target backscattering is somewhat low (weak targets or targets in shadow). On the other hand, spatial decorrelation is relevant only at large spatial baseline (let's say 150 m for ERS and Envisat case) over homogeneous scenes. This noise contribution can be tackled, by limiting the baseline, or reduced by ad-hoc filtering techniques.

Temporal decorrelation is a much more critical issue that strongly impacts the final monitoring in terms of spatial coverage. Qualitatively arid is much better than forest, dry conditions are better than wet, and long radar wavelengths are better than short ones. With respect to this aspect, application of the DInSAR technique to urban areas is particularly favourable. In such a case, due to the presence of stable and bright (manmade) targets, high correlation may be observed even at temporal separation of several years.

Atmospheric contribution shows correlation lengths on the order of 0.5-1 km spatial separation and together with DEM inaccuracy, which introduces errors in the topographic contribution cancellation for the generation of the differential interferogram especially at large baseline, represents a major limitation for the accuracy of standard two-pass DInSAR.

APS mitigation and the possibility to track the deformation $d(t_n)$, i.e. not only to determine its variation d between two time instants, and the retrieval of the residual topography Δz in (1.4), are the fundamental advances offered by recent multi-temporal DInSAR techniques over standard two-pass differential interferometry.

1.5 Summary

In this chapter, the basic theory of the SAR system and their interferometric applications have been introduced. Following a brief SAR history, the characteristics of SAR sensors and images are discussed. Finally, the basic rationale of the interferometric techniques is discussed emphasizing the application focused on retrieving earth surface displacements.

Chapter 2

Multi-temporal DInSAR Techniques

2.1 Introduction

Differential Interferometry is a technique for the detection of the Earth surface deformation and its basic principles have been discussed in the previous chapter.

DInSAR methodology has been firstly applied to investigate single deformation events. However, more recently, it has been also used to analyze the temporal evolution of the detected displacements through the generation of proper deformation time series, which have been obtained starting from a set of multiple differential interferograms. The interest on the development of these methodologies is testified by several algorithms, which have been already presented or that are under development. These approaches require that complex processing chains, with a given computational cost, are considered.

In the following, the rationale of the Small Baseline Subset (SBAS) approach [11] is presented. This technique has been extremely exploited in this PhD work.

2.2 Rationale of the Low and Full resolution SBAS-DInSAR Technique

In this paragraph, analytical details about the SBAS-DInSAR approach are provided, using the notation adopted by Berardino et al. (2002) [11]and Lanari et al. (2004)[12].

The Small Baseline Subset approach, allows investigating ground deformations at two distinct spatial scales referred hereafter to as large and local scale, respectively. At the large scale, the technique exploits averaged (multi-look) interferograms and allows us to generate mean deformation velocity maps and associated time series for areas extending for some thousands of square kilometers (up to 100 x 100 km), with a ground resolution of the order of 80 x 80 m. The obtained products are particularly suited for regional scale displacement analysis, but can be conveniently used to outline individual and multiple distant sites affected by ground deformation. At the local scale, the technique exploits the single-look interferograms, i.e., generated at full spatial resolution (typically of the order of 10 x 10 m), and leads to detection and analysis of local deformation.

Starting by assuming the availability of a set of $N+1$ SAR images for the same geographical area, acquired at the ordered times $(t_0,\ldots,t_N)$, and co-registered to a single image (referred to as "master" image), application of the standard SBAS technique starts with the generation of a number, M, of small baseline multi-look differential interferograms, which are then used for the evaluation of the spatially low-pass (LP) signal components. On these interferograms the retrieval of the original (unwrapped) phase signals from the modulo-2π measured (wrapped) phases is carried out. This operation, referred to as phase unwrapping, is based on the minimum cost flow algorithm [13], integrated with a region growing procedure to improve the performances in areas with low signal-to-noise ratio.

Considering the generic *k-th* unwrapped multi-look interferogram computed from the SAR acquisitions at times t_B and t_A, given by [11](Berardino et al., 2002):

$$\delta\phi_k(x,r) = \phi(t_B,x,r) - \phi(t_A,x,r) \approx \frac{4\pi}{\lambda}\left[d^{(LP)}(t_B,x,r) - d^{(LP)}(t_A,x,r)\right] + \\ + \Delta\phi_k^{topo}(x,r) + \Delta\phi_k^{atm}(t_B,t_A,x,r) \tag{2.1}$$

with

$$\Delta\varphi_k^{topo}(x,r) \approx \frac{4\pi}{\lambda}\frac{B_{n_k}\Delta z(x,r)}{r\sin\vartheta} \tag{2.2}$$

where: a generic coherent pixel of azimuth and range coordinates (x,r) is considered, $k \in (1,...,M)$, $\phi(t_B,x,r)$ and $\phi(t_A,x,r)$ are the multi-looked phase signals relevant to the two images used for the generation of the interferogram, and λ is the transmitted signal central wavelength. Moreover, in eq. (1), $d^{(LP)}(t_B,x,r)$ and $d^{(LP)}(t_A,x,r)$ are the LOS-projected LP components of the deformation at times t_B and t_A, with respect to the instant t_0 taken as reference and $\Delta\phi_k^{atm}(t_B,t_A,x,r)$ accounts for atmospheric inhomogeneities in the two acquisitions [14]. In eq. (2.2), B_{n_k} represents the perpendicular baseline component, ϑ is the SAR sensor look angle (about 23° for the ERS1-2 sensors) and $\Delta\phi_k^{topo}(x,r)$ accounts for possible topographic artefacts $\Delta z(x,r)$ in the DEM used for removing the topographic phase contribution within the interferogram generation process: note also that the noise effects are assumed negligible for the considered coherent pixel.

Eq. (2.1) and eq. (2.2) define a system of equations in the $N+1$ unknowns $\left[\phi(t_1,x,r),\cdots,\phi(t_N,x,r),\Delta z(x,r)\right]$ whose solution is obtained adopting the Singular Value Decomposition (SVD) method for each coherent pixel. For the inversion, no prior knowledge on the temporal artefacts of the investigated deformation is required.

After solving the system of eqs. (2.1) and (2.2), removal of the atmospheric phase artefacts $\Delta\phi_k^{atm}(t_B,t_A,x,r)$ is required to provide an

estimate of the deformation signal $d^{(LP)}(t_i,x,r)$, $\forall i=0,...,N$. The last step of the SBAS algorithm consists in detecting these possible atmospheric artefacts that are estimated by considering that the atmospheric phase signal component is highly correlated in space and poorly in time [15] [14]. Therefore, the "undesired" atmospheric phase signal is estimated from the computed time series by solving the system of equations (2.1) and (2.2), $\forall k \in (1,\cdots,M)$, through a cascade of a low-pass filter in the two-dimensional spatial domain followed by a temporal high-pass filter [11]

The extended SBAS full-resolution procedure is carried out in the following. In this case, from the application of the standard SBAS technique, the retrieved signal components are modulo-2π subtracted from the full-resolution interferograms; thus, the computed phase signal is related to the High Pass (HP) deformation and to the topographic phase components. The former, also referred to as "residual" deformation signal, is relevant to the localized deformation effects; the latter accounts for the local topography of the investigated pixels (for instance, the topography of the buildings) not considered in the DEM is used for the interferograms generation.

The residual phase of each coherent pixel within the *k-th* single-look interferogram can be expressed as [12] (Lanari et al., 2004)

$$\delta\Phi_k(x,r) \approx \frac{4\pi}{\lambda}\left[(t_B - t_A)\, v^{(HP)}(x,r) + \beta^{(HP)}(t_B,x,r) - \beta^{(HP)}(t_A,x,r)\right] + \\ + \frac{4\pi}{\lambda}\,\frac{B_{n_k}\,\Delta z^{(HP)}(x,r)}{r\,\sin\vartheta} \tag{2.3}$$

where: $v^{(HP)}(x,r)$ is the mean deformation velocity, $\beta^{(HP)}(\cdot)$ is the non linear component of the residual displacement and $\Delta z^{(HP)}(\cdot)$ is the local topography.

Inspection of eq. (2.3) allows for the following considerations. The atmospheric phase artefacts do not contribute to the HP signal components [15] [14]. A deformation signal decoupling into a linear and a nonlinear component is considered. This representation is related to the implementation of a specific procedure to unwrap the

residual phase signal. Phase unwrapping [12] is accomplished in two steps: first, an estimate of $\nu^{(HP)}(x,r)$ and $\Delta z^{(HP)}(\cdot)$ is performed; next, retrieval of the $\beta^{(HP)}(\cdot)$ signal component in eq. 3 is obtained through the Singular Value Decomposition (SVD) method. At this stage, coherent pixels have been identified on the full resolution SAR grid, where an estimate on the overall deformation (including the LP and HP components) and topography (including DEM artefacts and local topography) is available. The latter information can be used to precisely locate ("geocode") the coherent pixels.

On this final step several efforts have been spent in this work. In particular the exploited idea has been focused on properly combining the availability of a priori information on the topography of the investigated scene (SRTM DEM) with the local topography retrieved through the InSAR analysis. The overall topographic information allows us to accurately geocode the coherent SAR pixels by using standard geocoding tools. Accordingly we may use available codes and, at the same time , it allows us to easily integrate the InSAR result in GIS and to compare them with ground measurements and/or optical images.

A block diagram showing the SBAS-DInSAR procedure is portrayed in Figure 2.1

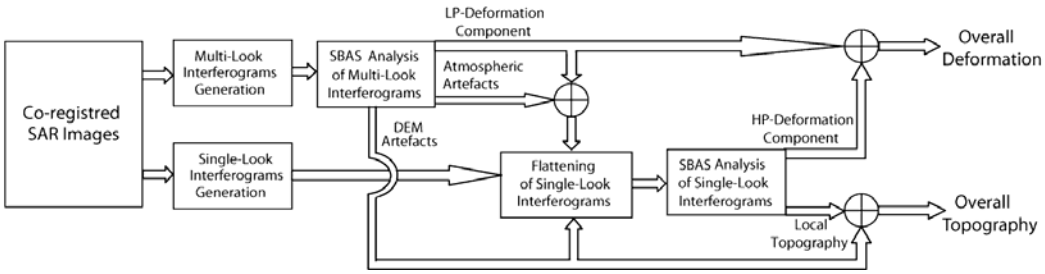

Figure 2. 1

Block diagram illustrating the SBAS-DInSAR technique.

2.3 East-West and Vertical deformation components

Availability of DInSAR results, computed from SAR data obtained from ascending and descending orbits, allows for the separation of the east-west (E-W) and the vertical components of the detected deformation [16] [17]. For all the coherent pixels common to both radar geometries, the sum and the difference of the mean deformation velocity computed for the ascending and the descending orbits are calculated. The sum is related to the vertical component of the ground deformation, whereas the difference accounts for the E-W component of the deformation. Because of the namely polar sensor orbit direction, the north-south (N-S) component of the deformation cannot be reliably singled out.

To explain the rationale for the retrieval of the E-W and the vertical components of the deformation, the following assumptions are made: (i) ascending and descending radar LOS directions (*LOS_Asc* and *LOS_Desc*, respectively) lay on the *east – z* plane, and (ii) the sensor look-angle ϑ is the same for both ascending and descending geometries. These are acceptable assumptions, given the problem. Let us take a point, say *P*, as the target "observed" from both the ascending and the descending satellite passes, and assume the availability of measurements relevant to the displacement components along the ascending (d_{LOS_Asc}) and the descending (d_{LOS_Desc}) radar LOS directions. Based on simple geometric considerations, the E-W component of the measured surface deformation, d_{East}, is:

$$d_{East} \approx \frac{\left(d_{LOS\_Desc} - d_{LOS\_Asc}\right)/2}{\sin(\vartheta)} \qquad (2.4)$$

and the vertical component of the measured deformation, d_z, is:

$$d_z \approx \frac{\left(d_{LOS\_Desc} + d_{LOS\_Asc}\right)/2}{\cos(\vartheta)} \qquad (2.5)$$

In figure 2.2 a geometric scheme to interpret the east-west and vertical deformation component is presented.

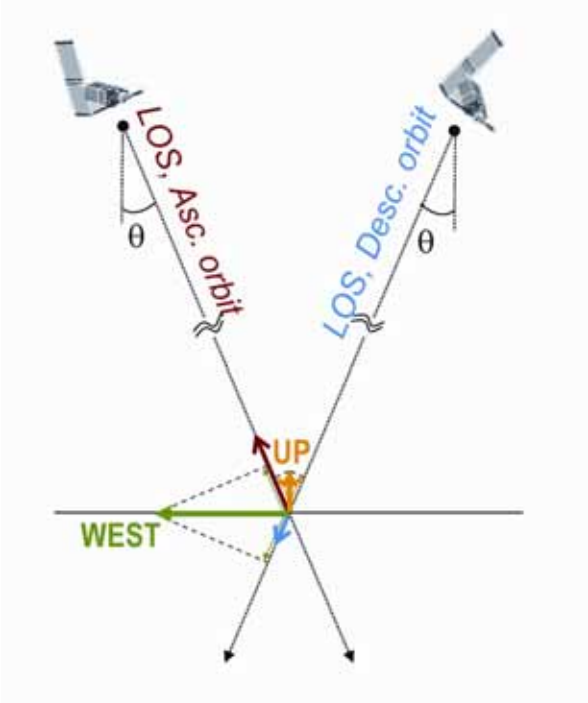

Figure 2. 2

Geometric scheme to interpret the deformation (green east-west component, yellow up-down component) detected through the SBAS-DInSAR technique with respect the measurements relevant to the ascending (red) and the descending (blue) radar LOS. θ is the satellite view angle.

2.4 Summary

The topic of this chapter concerns the extension of the basic DInSAR methodology to exploit the temporal evolution of the deformation by using a set of multiple differential interferograms through the generation of proper deformation time series. In particular the Small Baseline Subset (SBAS) approach rationale is presented.

The SBAS approach enable to investigate ground deformations at two distinct spatial scales, referred hereafter to as large and local scale, respectively. At the large scale, the technique exploits averaged (multi-look) interferograms and allows to generate mean deformation velocity maps and associated time series for areas extending for some thousands of square kilometers, with a ground resolution of the order of 80 x 80 m. The obtained products are particularly suited for regional scale displacement analysis, but can be conveniently used to outline individual and multiple distant sites affected by ground deformation. At the local scale, the technique exploits the single-look interferograms, i.e., generated at full spatial resolution (typically of the order of 10 x 10 m), and leads to detection and analysis of local deformation related to man-made structures and single building.

Finally, starting from DInSAR results computed from SAR data obtained from ascending and descending orbits, it is also shown how the separation of the east-west (E-W) and the vertical components of the detected deformation [16] [17] is achieved.

Chapter 3

Use of the SBAS-DInSAR Algorithm for Surface Deformation Analysis

3.1 Introduction

In the scientific literature an increasing number of case studies dealing with the monitoring of displacements of both landslide and subsidence phenomena propose the use of innovative remote sensing techniques. This could be ascribed to the need of complementing the traditional techniques with both less expensive and time consuming systems providing a large amount of data over large area with comparable accuracy. A wide range of remote sensing techniques for measurements of the surface topography can be used such as aerial-photogrammetry, G.P.S., LIDAR, optical fibers, DInSAR, etc.

Amongst innovative techniques for ground surface displacement monitoring the use of advanced satellite techniques can be extremely useful. In particular, the differential SAR Interferometry (DInSAR) can complement with traditional topographic techniques as well as GPS and LIDAR to obtain measurements of ground surface displacements while being less expensive and time consuming [18].

This PhD thesis represents one of the first examples of extensive use of DInSAR technology devoted to the subsidence phenomena and hydrogeological instability analysis. The results are significant, because they prove the feasibility of a region-wide, satellite-based system for monitoring multiple, potentially hazardous natural and human induced processes over large areas. Moreover it is also shown the capability of such techniques to carry out investigation at the scale of single buildings

The availability of updated displacement monitoring datasets can provide useful information concerning both the spatial and temporal evolution of the single phenomenon as well as the detection of new ones. Accordingly, the main result could be the continuous updating of subsidence/landslide maps. Nevertheless, displacement monitoring could allow singling out most critical areas in which detailed surveys to structures and infrastructures are worth being concentrated.

Several results obtained by applying the two scale DInSAR-SBAS approach (discusses in the previous section) in selected case studies relevant to subsidence phenomena and landslides areas affecting the Middle and Southern Apennines, will be presented in the next chapters. These analyses are carried out by using multilook DInSAR interferograms with a spatial resolution of the order of 80x80 m, in the low-resolution approach and with a spatial resolution of the order of 10x10 m in the full resolution one, computed both from SAR data acquired by the ERS-1 and ERS-2 sensors. Case studies reveal the peculiarities of the SBAS technique and its surface deformation retrieval capability for what concerns both large-scale deformation phenomena and more localized displacement effects.

In the following two sections, a brief description of subsidence and landslide phenomena will be proposed.

3.2 Subsidence phenomena

Subsidence may rank as one of the most widespread ground hazard. The seriousness of this hazard was recognized by the United Nations Educational, Scientific and Cultural Organization (UNESCO) in 1969, when this problem was first included for study under the International Hydrological Decade (IHD) and, later, the International Hydrological Programme (IHP). The efforts of the scientific community have been essentially directed toward: furthering the knowledge on both natural and anthropogenic causes; understanding of mechanisms and related effects; the development of reliable field measurements and laboratory tests; the implementation of prediction

models and the planning of monitoring systems and remedial measures.

With reference to subsidence phenomena, the availability of absolute settlement measurements can enable, at different scales, the detection of areas most prone to subsiding. In this regard, it is often assumed that uniform soil subsidence will not lead to structural damage to buildings. Since the foundation will simply subside together with the soil. However, a shallow foundation, with its base below the groundwater level, may lose part of its bearing capacity when the soil surface subsides and the groundwater level does not change. Accordingly, if the foundation of a given structure is non-uniformly loaded this may lead to non-uniform settlements of the foundation and possible damage to the superstructure as well. If settlement spatial gradients are considered, the obtained information can be used to detect the portion of most prone areas where severe effects in terms of damages to buildings, if any, can occur. Indeed, the higher the differential settlements are the more severe the damage to buildings can be. Consequently, a building located on the border of a subsidence bowl is expected to be more damageable than an analogous building entirely located within the subsidence bowl. These data could turn out to be useful to single out the areas where detailed studies need to be carried out in order to collect the necessary information for both the interpretation of the phenomenon and the generation of thematic maps which can be used for built-up area management.

The available scientific literature on subsidence phenomena highlights that these results are difficult to obtain over large areas due to the limited number of monitored points inside the affected areas. This is essentially related to the most frequently used conventional settlement measurement techniques, i.e. levelling surveys often coupled with GPS measurements or monitoring of fissures in the earth or building crack opening. These technique, although very precise, turn out to be rather expensive and time consuming if used over large areas.

In the following, the definition of subsidence phenomena and their more frequent causes are briefly presented.

3.2.1 Definition and causes

Land subsidence is the lowering of the ground surface elevation induced by changes taking place underground. It may be often considered as the measurable effect – in terms of magnitude, rate and spatial distribution – of the concomitant occurrence of various causes, either natural or artificial. These can result in: a variation of the effective stress levels in involved soil deposits related to pumping fluids and gas from either underground reservoirs or underground

Type	Result	Cause
Natural	Compaction of surficial soils	Hydrocompaction of dry soils on initial wetting.
		Compaction of organic soils on drainage.
	Rapid local subsidence	Sinkholes in karst terrain.
		Collapse feature over salt.
	Long-term regional subsidence	Compaction of basin sediments.
		Tectonic influences.
Anthropogenic	Rapid local subsidence due to subsurface mining	Collapse of underground coal mines, salt mines, limestone mines.
		Impact of engineered underground openings such as tunnels.
	Long-term regional subsidence due to withdrawals of fluids.	Groundwater withdrawals
		Oil and gas production.
		Geothermal development.
		Mine dewatering
Mitigating Factor	Long-term regional impact on coastal environment	Sea-level rise due to global warming.

Table 3. 1

Definition and causes of land subsidence

excavations; the degradation of soil mechanical properties due, for instance, to groundwater pollution. However, sometimes different concurrent causes can originate a subsidence phenomenon, thus

making it difficult to individuate the role played by each of them; consequently, it may be not easy to relate causes and consequence effects. The recognized causes of land subsidence as both natural and anthropogenic can be distinguishes between cases of rapid local subsidence and long-term regional subsidence. The latter can occur naturally, due to sediment compaction or anthropogenically, due to the withdrawals of fluids from the subsurface. (Table 3.1)

Particularly, the economic losses are related to six different anthropogenic causes of land subsidence such as: pumping water, oil, and gas from underground reservoirs; dissolution of limestone aquifers (sinkholes); collapse of underground mines; drainage of organic soils; natural compaction and initial wetting of dry soils.

In Italy and all over the world the consequences on the environment and, in particular, the damages caused by subsidence phenomena to buildings and infrastructures are always extremely expensive due to the large extension of the involved areas.

3.3 Landslide Phenomena

Landslide denotes the movement of a mass of rock, debris or earthdown a slope.

Landslides are one of the most serious natural hazards in terms of casualties and economic impact, besides their interaction with many other natural phenomena. Hence, both the organisms entrusted with the safeguard of the population and the scientific community are strongly committed to reduce their effects. However, achieving significant results in this field is not a simple task for many reasons such as the intrinsic complexity of landslides and the geological environment where they take place. In this regard, difficulties arise since landslides often involve highly heterogeneous soils and rocks; moreover they are characterized by space- and time-dependent mechanisms, which are not easily recognizable at either small or large scale.

A universal classification of landslides does not exist. Moreover, the influence of geological and topographic conditions frequently cause the real phenomenon to be a combination of two or

more mechanisms produced either in simultaneous process or in successive and interconnected processes. As a consequence, a huge and clear knowledge of the possible behaviour of a soil/rock mass is a fundamental step of the study; this latter, in turn, can be enriched through field trips and analyses of as many case histories as possible. Once familiarity is attained, analysis of existing classifications becomes easier.

Owing to the complexity of these instability phenomena, investigations and studies devoted to landslides analysis pursue different aims: the editing of inventory maps; the definition of soil/rock mechanical properties via in situ or laboratory tests; the setting up of geological/geotechnical triggering and evolution models; monitoring and control, and so on.

The present Thesis work essentially focuses on the analysis of ground surface displacements of slow-moving phenomena. According the principal types of such phenomena include translational slides and earth flows, mainly involving stiff clays and clay shales. Moreover, deep-seated gravitational slope deformations and creep phenomena can be also considered.

To properly interpret the results deriving from displacement analyses, an in-depth knowledge of mechanisms characterizing the stage of movements of slow-moving landslides seems to be of particular concern.

Despite limitations, largely due to the 35-days acquisition repeat cycle and the C-band operating frequency of the exploited radar sensors on board the ERS-1/2 satellites, the SBAS-DInSAR technique produced maps and associated time series of deformation that allowed for the successful investigation of geophysical, geomorphological, and human induced processes that may result in hazardous conditions to the population.

3.4 Summary

This chapter introduce the SBAS-DInSAR tecnique that has been applied in the following sections for the analysis of different ground surface deformation. In particular, the possibility to exploit the SBAS technique for the analysis of subsidence and landslide phenomena in case studies relevant to the Middle and Southern Apennines areas has been introduced. Furthermore, a brief description of the subsidence and landslide phenomena, from geological point of view, has been reported as well.

Chapter 4

Surface Deformation Analysis in Basilicata region

4.1 Introduction

This chapter is focused on a DInSAR survey carried out on a Basilicata region (Italy) area, and SAR data acquired by the ERS-1/2 sensors on descending orbits in the time interval 1992-2000 were used. This analysis was carried out by applying the Small Baseline Subset (SBAS) algorithm [11].

In particular, the DInSAR mean deformation velocity maps analysis allows to detect an unknown ground deformation effect which involves the urban area of Satriano di Lucania, located close to Potenza and to analyze the temporal evolution of the well-known gravitational phenomena affecting the Maratea valley.

4.2 Geological and geomorphological setting

The large part the Satriano di Lucania area is covered by the terrains of the Monte Facito Formation (Figure 4.1a). This formation consists of terrigenous deposits, such as fine to coarse re-sedimented carbonates and clayey-sandy material, associated with a calcareous member composed of large fractured limestone blocks, nodular limestones and radiolarites The terrigenous member is frequently covered by clay-rich debris and landslide material; moreover, near the banks of the Melandro river, alluvial deposits can be found. The bedrock, composed of marls intercalated with calcarenitic material (terrigenous member of Monte Facito Formation), can be found at a depth varying within the range: 7-15 m. In particular, in the built up area the thickness of the debris reaches a maximum depth of 13 m. Moreover, the old town of Satriano di Lucania is located on the left bank of the Melandro river which is the main tributary of the Sele

river. The Melandro river represents the main drainage-structure for the shallow and deep waters of the built up area and it has been modified by the landslides affecting the

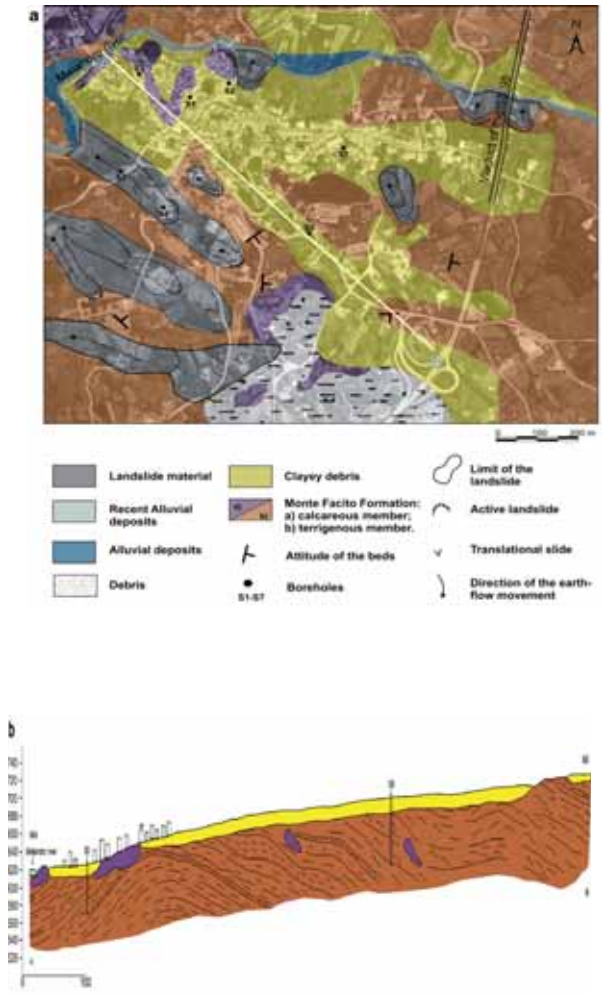

Figure 4. 1

Maps relevant to the Satriano di Lucania area: (a) geological and geomorphological map superimposed on an orthophoto of the zone; (b) geological cross-section along the path marked by the continuous segment AB

near slopes due to the erosion produced by the river. At variance of these phenomena, the translational slides affecting the SW area of the town and surroundings have been re-started by the 1980 Irpinia earthquake and evolved into earth-flow phenomena[19].

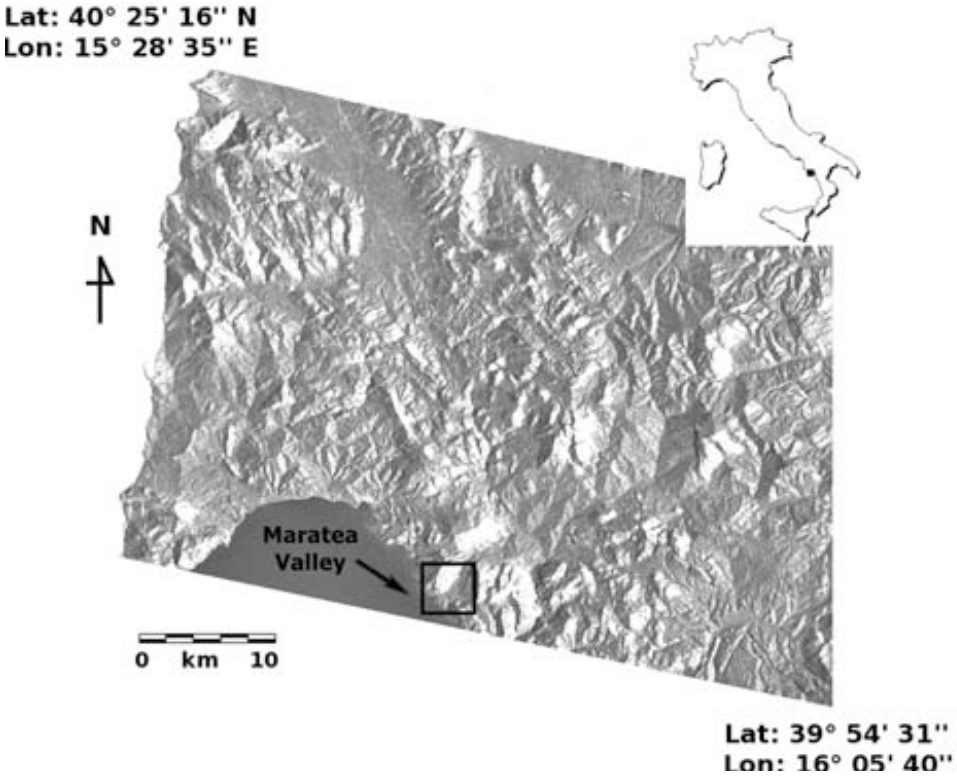

Figure 4. 2

SAR image of the southern part of the Basilicata Region (Italy) where the black box identifies the investigated Maratea Valley. The inset in the upper right corner shows the location of the area.

The Maratea Valley (see Fig. 4.2), is located on the Thyrrenian Coast of the Basilicata region (southern Italy) and is a Quaternary pull-apart basin.

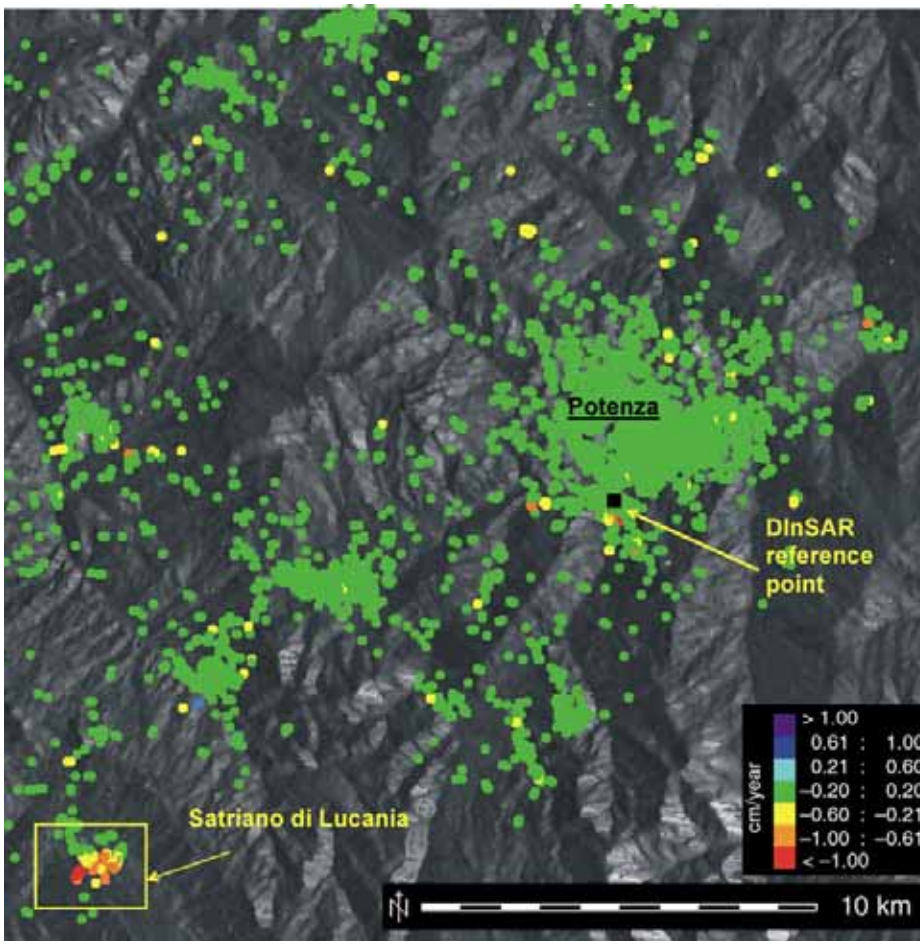

Figure 4. 3

DInSAR sensor line of sight mean deformation velocity map superimposed on the grey scale SAR intensity image of the studied area. The yellow rectangle highlights the Satriano di Lucania town, which is affected by a deformation phenomenon. The black square represents the DInSAR reference pixel.

This site is characterized by important gravitational phenomena, formerly indicated as sackung and by strong superficial debris landslide affecting, respectively, the Mesozoic carbonate-dolomite formations and clayey-marly flyschoid terrains The most important tectonic lineament is the overthrust of the Bulgheria-Verbicaro Unit (BVU) on the highly tectonized and chaotic clayey-marly flysch, in black-shales facies (Crete Nere Formation, Cretaceous-lower Eocene). The Crete Nere argillitic flysch, under the

assumption of a plastic behavior caused by high water content, is in the presence of tectonic stresses and represents a lubricant for deep gravitational movements. Geological surveys, previously performed in the area, show a litostratigraphic setting characterized by calcareous materials of the BVU, dislocated by gravitational phenomena and positioned on a clayey-marly substratum.

The thickness changes from 3 to 148 m and the piezometers show the presence of a ground water flow confined at the bottom by the Liguride Unit.[20]

4.3 DInSAR analysis

4.3.1 Satriano di Lucania Area

This analysis involved 60 SAR images and led to detect an unknown ground deformation effect which involves the town of Satriano di Lucania, located about 20 Km from the town of Potenza. In figure 4.3 the computed LOS mean deformation velocity map relevant to the investigated area is presented. [19]

In order to better understand the detected displacements a 3D view shown in Figure 4.4a the DInSAR LOS mean deformation velocity map superimposed to an orthophoto of the zone, with highlighted topographic contours (with a 25 m spacing).

On the basis of Figure 4.4a some key considerations can be carried out. First, most of the coherent pixels are related to urbanized zones and man-made structures, such as the viaduct of the main road SS.95 “Tito-Brienza” (built up during the 80’s) that is located in the lower left corner of the image. In this case the only significant exception is represented by a non coherent zone within the central part of the Satriano town where building has been carried out, that is very likely responsible for the coherence loss.

Concerning the detected deformation, the displacements affecting the SW zone of the map (red circles in the white dashed box) occur within the previously mentioned landslide bodies reactivated following the 1980 Irpinia earthquake. In this case the DInSAR analysis reveals the active behavior of these landslides with deformation rates that exceed, in some cases, 1 cm/year. The temporal evolution of the measured deformation for the sample DInSAR pixels marked by b and c in Figure 4.4a are shown in the associated plots of Figures 4.4b and 4.4c, respectively. In this case, the deformation time-series show rather continuous displacement trends.

Although the highest deformation rates are those within the above discussed landslides, the most peculiar deformation pattern is the one affecting the urbanized area of the town. This effect, showing spatially varying deformation characteristics, was previously unknown and is discussed in detail in the following analysis. In particular, the deformation involves a sort of triangular-shape area (see Figure 4.4a) including terrains belonging to the clayey debris and, in some cases, to

the terrigenous member of the Monte Facito Formation; on the contrary, the north-western

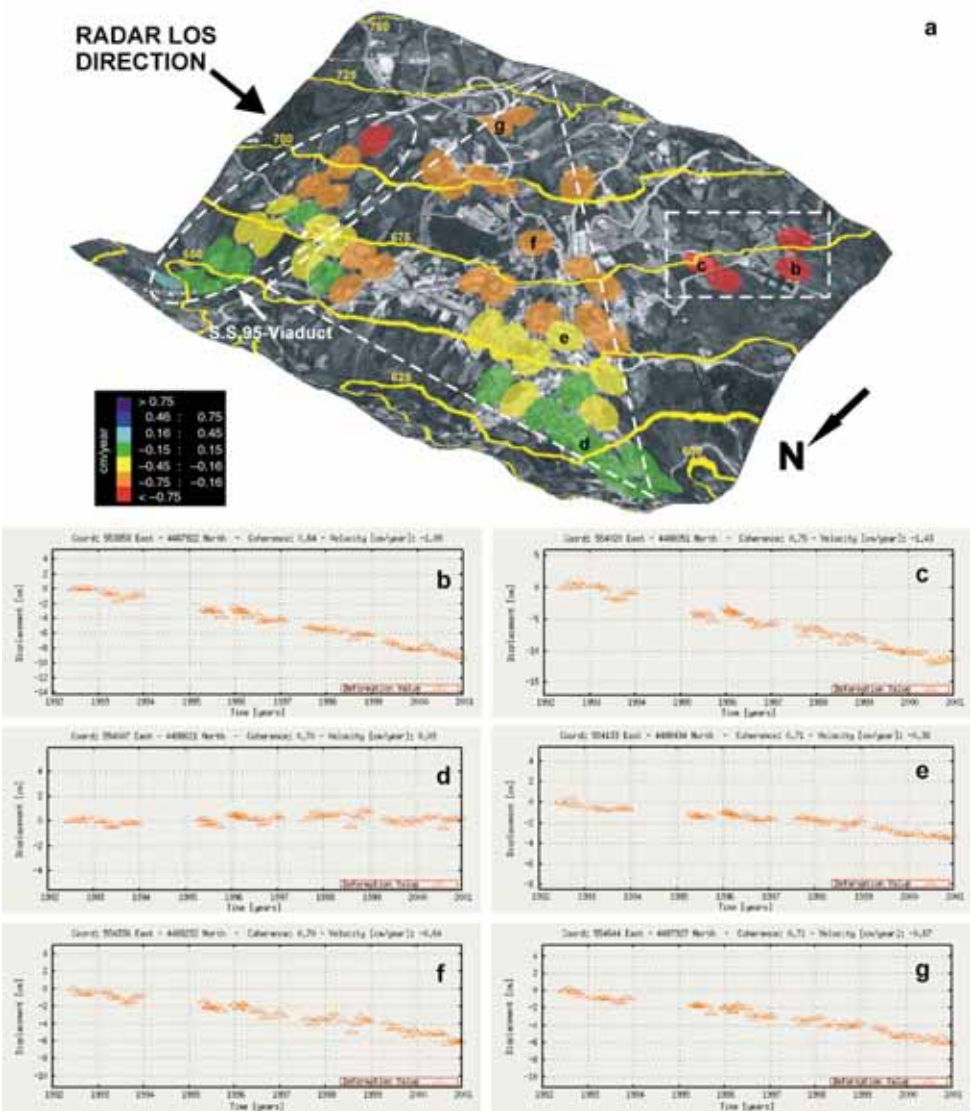

Figure 4. 4

DInSAR LOS deformation measurements: (a) three-dimensional representation of the DInSAR mean deformation velocity (in cm/yr) map superimposed on an orthophoto of the zone that is the same shown in Fig. 4.1a. The three main deforming areas have been highlighted with a dashed white rectangle, triangle and ellipse, respectively. The Figure also reports the topographic contours (in yellow) of the zone and the location of six pixels whose deformation time-series plots are presented in the following Fig. 4.4b–g; b–g) plots relevant to the SAR pixels identified in Fig. 4.4a as b–g, respectively.

part of the city, where the calcareous member of the Formation outcrops, appears to be stable.

However, the sign of the deformation clearly shows that an increase of the sensor-targets range has been detected. By considering the radar LOS direction and the topography characteristics of the area, it appears that the detected deformation effect is correlated to the topography variations

In order to further investigate the characteristics of this displacement pattern, in Figures 4.4d-4.4g the plots of the deformation time-series corresponding to the pixels labeled from d to g in Figure 4.4a, presenting stable to deforming trends, respectively are shown. Based on these measurements, the detected deformation exhibits a rather continuous displacement behavior.

A second area, where a space-variant deformation pattern can be detected, is the zone relevant to the location of the previously mentioned viaduct of the main road SS.95 (highlighted by the white dashed ellipse in Figure 4.4a). In this zone the contributing pixels are mostly those relevant to the viaduct that dominates the back-scattering characteristics of the SAR signals. Concerning the detected displacements, in this case the deformation shows a rather continuous trend and the displacement pattern seems again to be correlated with the topography of the area. However, by considering the viaduct orientation as well as the topographic gradient direction, it is evident that they are nearly orthogonal to the sensor line of sight (see Figure 4.4a). Accordingly, the deformation occurring along this direction does not significantly contribute to the LOS displacement component measured via the DInSAR technique and the observed deformation are due to the vertical displacement component.

4.3.2 Maratea Valley

In Figure 4.5a the estimated mean deformation velocity map in the radar LOS that provides key information on the detected displacement pattern, is presented. In this case the coherent SAR pixels, represented by circles, have been superimposed on an orthophoto of the zone; and the color of each SAR pixel identifies its mean deformation velocity amount. By observing Figure 4.5a, it is evident that the investigated area shows slope instability movements of significant magnitude reaching a maximum deformation velocity of about 3.3 cm/year during the time interval studied. In order to analyze, in addition to the mean deformation characteristics, also the temporal evolution, in Figures 4.5b–4.5g the plots relevant to the deformation time series for a selection of coherent SAR pixels are presented.

These sites have been chosen due to their features in the corresponding time series and also because they are relevant to ground points, identified by blue squares in Figure 4.5a, where GPS measurements were available from campaigns carried out in June 1997, November 1999 and March 2000. [20]

Accordingly, a comparison between the geodetic and the SAR measurements by projecting the former in the radar LOS and superimposing the results on the corresponding DInSAR measurements is carried out (see Figures. 4.5b–4.5g). Although a quantitative analysis is not appropriate in this case, due to the limited amount of available GPS data, it is rather clear from Figures 4.5b–4.5g that the geodetic and DInSAR measurements are consistent

By further observing these time series, an interesting observation can be also carried out. Indeed, the deformation time series generally reveal the presence of temporal changes in the velocity of the landslide movements. In particular, it appears that after a nearly constant deformation rate of up to a few cm/year in the mid–1990s, during the 1995–1996 and 1999–2000 time intervals the landslide movements significantly slowed; a similar trend is also generally revealed by the available GPS observations.

Finally, in the context of landslide monitoring, the orientation and/or the slope of the investigated area may play a key role in the analysis. Indeed, the landslide could even be not ‘‘visible’’ by the SAR sensor just because of the geometric distortions, intrinsic to the

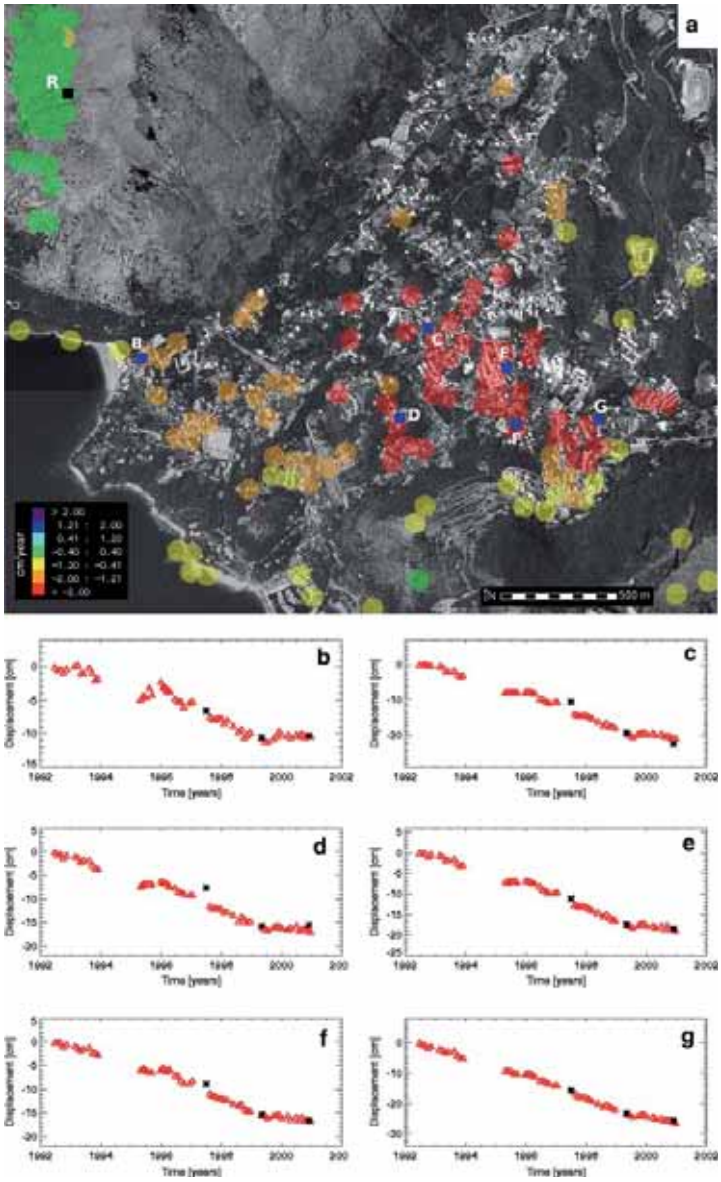

Figure 4. 5

DInSAR results relevant to the Maratea Valley: a) orthophoto of the investigated zone superimposed with the LOS mean deformation velocity map in correspondence of the coherent SAR pixels (color circles); the locations of the points where GPS measurements have been investigated (blue squares in correspondence of the pixels labeled B, C, D, E, F and G) also have been highlighted; b-g) comparisons between the DInSAR time series (red triangles) and the GPS data (black stars) for the pixels labeled B, C, D, E, F and G in Figure 4.5a, respectively. Note that the GPS measurements have been projected on the radar LOS.

side-looking radar imaging characteristic of the system. In any case, it

is evident from the results presented, the capability of the SBAS technique to identify changes in mobility for landslides with the characteristics of the Maratea Valley where a very significant urbanization is present.

4.4 Summary

The SBAS DInSAR technique has allowed to detect a completely unknown deformation phenomenon which involves the urban area of Satriano di Lucania (southern Italy), showing a complex space-variant pattern. Although the most peculiar deformation pattern is the one affecting the urbanized area of the town, this effect, shows spatially varying deformation characteristics. In particular, the SBAS DInSAR results has permitted to discriminate three main areas characterized by different deformation pattern.

In the Maratea Valley case study it is evident that the investigated area shows slope instability movements of significant magnitude reaching a maximum deformation velocity of about 3.3 cm/year. A further observation of the SBAS-DInSAR time series, reveals the presence of temporal changes in the velocity of the landslide movements. In particular, it appears that after a nearly constant deformation rate in the first period of the studied time interval, in the second one the landslide movements significantly slowed

In this case, it is evident, in the context of landslide monitoring, the capability of the SBAS technique to identify changes in mobility for landslides with the characteristics of the Maratea Valley.

Chapter 5

Two scales SBAS-DInSAR technique to investigate subsidence phenomena:the city of Sarno case study

5.1 Introduction

In this chapter the SBAS-DInSAR technique to investigate subsidence phenomena in urban areas and, thus, to provide useful information for the detection of building damage susceptibility is presented. With reference to the Sarno town (Italy), whose urban area is affected by ground surface settlements ascribed to groundwater withdrawals, results at low and high resolution, obtained by using data acquired by ERS-1/2 satellites in the period from 1992 to 2004, are shown.

5.2 Sarno urban area test site

Sarno urban area (around 30,000 inhabitants) is located in the coastal graben of the Campanian Plain, Italy, extending for almost 170 km^2, bordered to the south by the carbonatic ridge of Lattari Mountains, east by the Sarno Mountains and north by the volcanic complex of the Somma-Vesuvius (Figure.5.1). Due to intensive agricultural activities as well as numerous food industries, all over the highly urbanized Campanian Plain, the water demand for different uses constantly increased during the last century resulting in intensive, and sometimes uncontrolled, massive withdrawals.

The exploitation of Campanian Plain's rich water resource started since the 1940s with the construction of numerous deep wells;

then, by the end of the Second World War, some more huge water-catchments were built, essentially in the Lufrano zone (Figure.5.1). A similar intensive exploitation of the underground water resource has been carried out in Sarno area since 1960 by means of both public works built in close proximity to natural springs and private withdrawals, with a basically seasonal use, ranging up to $30x10^6$ m^3/year.

The captation works, either inside or outside Sarno area, caused a marked lowering of the groundwater table within the urban area. Detailed investigations were carried out more than ten years ago [21] and the results highlighted the relationship between lowering of the groundwater table and field surface settlements, the magnitude of which is strictly related to the presence of lenses or layers of very deformable peat within the superficial deposits.

Figure 5. 1

Campanian Plain (Campania Region, South Italy) and test site.

5.3 DInSAR analysis

In order to investigate several aspects of subsidence at different scales, low and full resolution processing were performed by processing 83 SAR data of the ERS1/2 satellites between 1992 and 2004 (descending passes; track 36, frame 2781).

The validation of the SAR data was achieved via a point-wise comparison with traditional ground leveling (mean square deviation of 0.3 mm/km) data referring to a net of 18 benchmarks, some of them corresponding to the heads of boreholes equipped with piezometers

5.3.1 Low resolution DInSAR analysis

Ground settlements obtained by the DInSAR processing were compared to the results provided by ground leveling data. Figure 5.2 shows a map of the benchmarks (marked by squares) and of the centers of the achieved coherent SAR pixels (marked by triangles) superimposed to an orthophoto of Sarno town area.

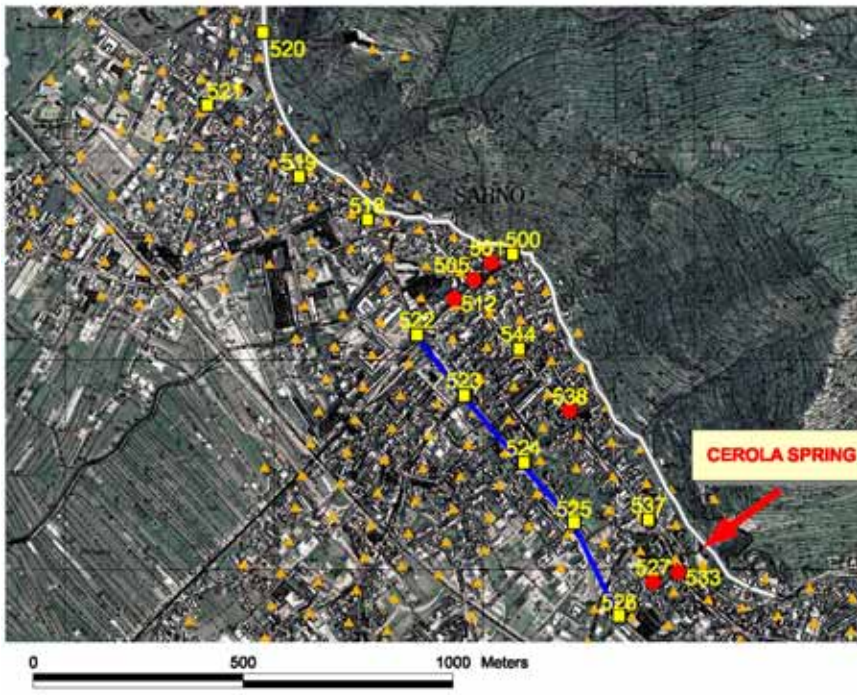

Figure 5. 2

Sarno Town study area

Figure 5.3 shows a comparison between low-resolution DInSAR data and leveling results, in terms of settlements evolution in time, with reference to four ground leveling benchmarks. Particularly, the four selected

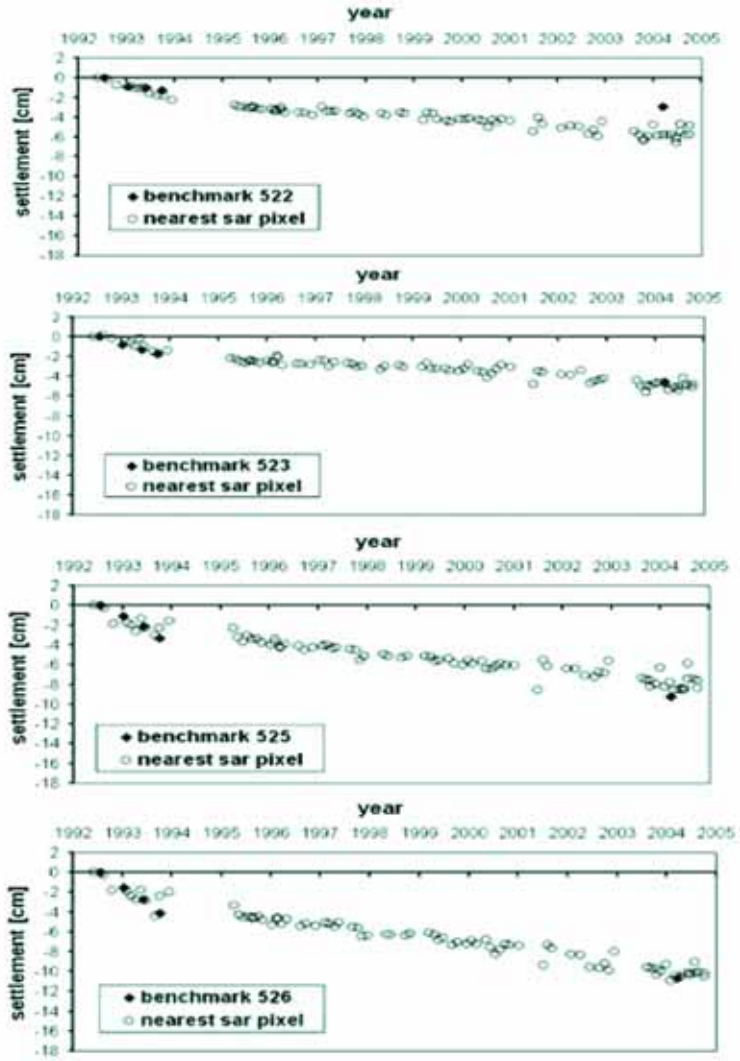

Figure 5. 3

Settlement point-wise comparisons (from low resolution SAR and ground leveling data).

circular SAR pixels (80 meter diameter) are the closest to each single benchmark and their vertical components, corresponding to the measured LOS deformations, were computed assuming that the displacements mainly occurs along the vertical direction.

The results obtained for the period 1992-1993, when the highest settlement rates occurred (Fig. 5.3), show a good fitting so confirming the above assumption. Furthermore they also highlight that remotely sensed settlements increase almost linearly in time from the beginning of 1995, reaching cumulative values that again fit well the most recent available leveling measurements (March 2004). This result agrees with the spatial distribution of cumulative ground settlements [22] whose magnitude increase where the thickest peat layer was recovered [21].

As far as the relationship between the magnitude of settlements (both absolute and differentials) and the building damage occurrence is concerned, a first attempt at "urban scale" [22] who used low resolution DInSAR data referring to the urban area of Sarno.

In particular, deformation gradient map was computed on the ground pixel grid starting from low-resolution DInSAR measured settlements and then it was compared with the localization of damages mainly recorded to masonry buildings with shallow foundations

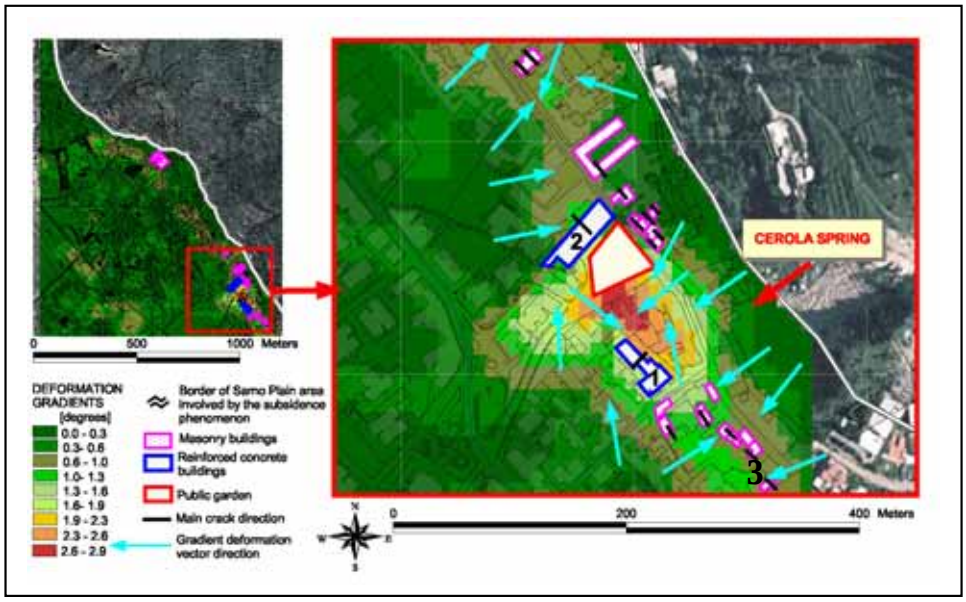

Figure 5. 4

Deformation gradient map of the investigated area and spatial distribution of damaged buildings

(Figure 5.4). First of all, Figure 5.4 clearly shows that damaged buildings (framed either in blue or in magenta, according to their structural typology) are all located within a narrow strip, almost parallel to Sarno mountains [21], where the highest settlement gradients are attained. The recorded damages essentially consist of i) noticeable rigid tilts between adjacent buildings (Figure 5.5) or ii) sub-vertical cracks – whose width increases from the bottom to the top – as in the case of the ancient low-rise masonry building with shallow foundations (Figure 5.6) labeled with the number 3 in Figure 5.4. Outside the critical zone, only one reinforced concrete building (Figure 5.5), signed by the number 2 in Figure 5.4, has experienced a sub-vertical crack in correspondence of a “weak” section.

Figure 5. 5

Damages to the reinforced concrete building (labelled with n.1 in Figure 5.4) located in the proximity of the Cerola zone (photo dated July 2004).

Other interesting results arise referring to the open cracks, monitored in some damaged buildings with the aid of displacement transducers from October 1992 to September 1993. These cracks progressively increased during the period (June 1992 - November 1993) [21] which the map of Figure 5.4 refers to. Furthermore, it is interesting to point out that both cracks and axes of building rotation are almost always normal to gradient deformation directions, shown in Figure 5.4 as arrows.

Finally, the absence of damages to some buildings located where significant displacement gradient values are present, is not surprising for several reasons. Inside this critical zone, buildings are essentially on reinforced concrete and more recent than the aforementioned masonry buildings. In addition, a large portion of the zone is occupied by a public garden (red framed in Figure 5.4).

Although not pursuing the complex problem of building damage forecasting in subsiding areas, the obtained results show that the use of low-resolution DInSAR data can support, at municipal scale, valuable considerations on the spatial distribution of damages to buildings.

In addition, the analysis of settlement gradients can allow some preliminary evaluation of the damage characteristics, i.e. the direction of cracks as well as of the axis rotation in the case of rigid tilt,

Figure 5. 6

Damages to the masonry building (labelled with n. 3 in Figure 5.4) located in the proximity of the Cerola zone (photo dated July 2004).

suffered by different typologies of buildings [22]. In this regard, the significant contribution offered by full-resolution DInSAR data analysis is discussed in the following section.

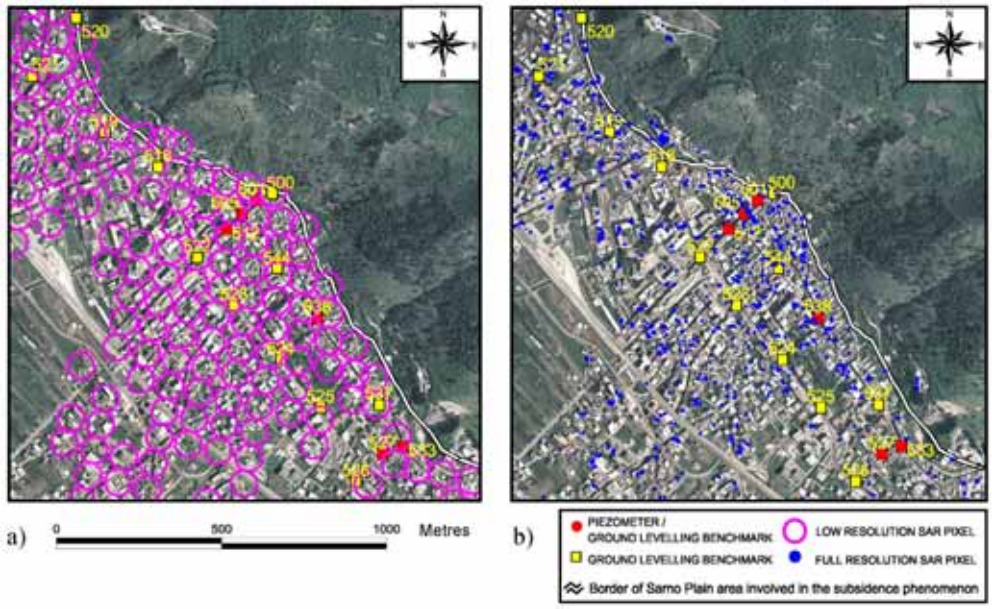

Figure 5. 7

Maps of Sarno Town study area: localization of ground levelling benchmarks and coherent SAR pixels at both low (a) and full (b) resolution

5.3.2 Full resolution DInSAR analysis

A further step towards the testing of DInSAR technique in subsidence induced ground deformations analyses concerns the full-resolution analysis. The following section, discussing the peculiar features of full resolution data, highlights the different aspects to be investigated when dealing with "at building scale" analyses [18] within Sarno town.

5.4 Comparison of DInSAR data distribution at low- and full resolution.

A key point of full-resolution DInSAR data is the precision in

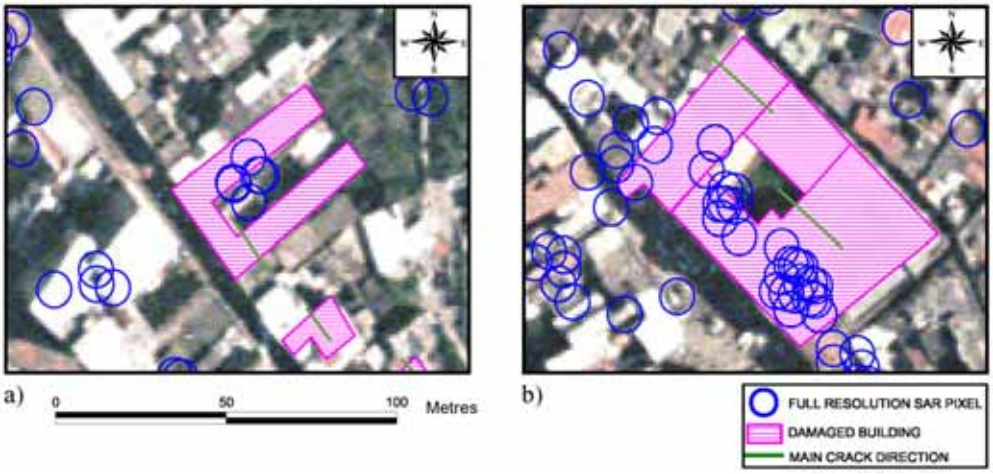

Figure 5. 8

Close-up view of the spatial distribution of coherent SAR pixels detected at full resolution on damaged buildings: a) building on reinforced concrete; b) a masonry structure building

estimating the residual topography thus allowing accurate geo-localization of the monitored pixels. Figure 5.7a shows a map of low-resolution DInSAR coherent pixels which exhibit a regular spatial distribution covering almost uniformly the urban area of Sarno town. On the other hand, full-resolution DInSAR pixels concentrate (Figure 5.7b) on elements where the signal attains the highest coherence (mainly building in urban areas).

Frequently, several full-resolution SAR pixels are available for the same building roofs (Figure 5.8) so allowing the detection of local effects induced by the subsidence phenomenon.

Similarly to low-resolution data, full-resolution DInSAR ones were firstly validated via a comparison with geodetic data. In Figure 5.9 two settlements vs. time diagrams are shown with reference to the same sample of benchmarks chosen for low-resolution data validation (Figure 5.3).

The diagrams confirm that a good fitting of topographical leveling measurement can be achieved, independently from the different size of DInSAR coherent pixel area.

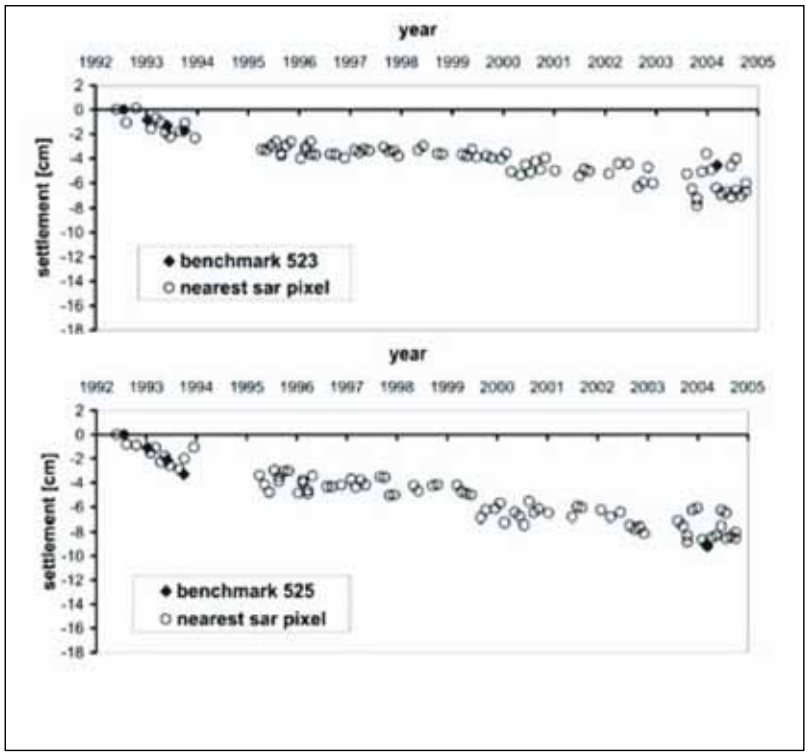

Figure 5. 9

Settlement point-wise comparisons from ground levelings and full resolution DInSAR data).

5.5 Summary

This chapter has been focused on the application of DInSAR to a classical geotechnical problem concerning a subsidence phenomenon occurring in Sarno urban area, emphasizing the related effects in terms of the spatial distribution of damage to some buildings. Although the scenario is rather complex because it involves several factors (water

withdrawal, thickness of deformable soil layers, building typologies, etc.), the obtained results showed that the applied SBAS-DInSAR approach can be a valuable tool to detect critical areas affected by noticeable settlement.

Interesting correlations between the direction of the detected ground deformation gradients and some building damage characteristics were also made.

Although in the presented analysis is not meant to explain the whole complex problem of building damage forecasting in subsidence-affected areas, it clearly demonstrates that use of multi-look DInSAR products allows meaningful investigation of the peculiarity of recorded damage characteristics. For example, the directions of cracks as well as of the axis of rotation in the case of rigid tilt, involving, at a larger scale, ancient low-rise masonry buildings, were detected.

In addition, the available field-measured data indicate that, for this case study, there is a strong correlation between the amount of pumped groundwater and the groundwater level in the aquifer and, in turn, between this and the settlement rates. Moreover, these latter effects seem larger where the most deformable peat strata are thicker.

Finally, the obtained results support the application of DInSAR monitoring to hazard analysis and risk mitigation strategies, including groundwater resource management.

Chapter 6

Low and full resolution DInSAR data analysis: the city of Rome case study

6.1 Introduction

In this chapter the analysis of surface deformation at two distinct spatial scales: a low resolution large scale, and a fine resolution local scale on the city of Rome (Italy) is presented.

At large scale, the technique allows to generate mean deformation velocity maps and associated time series for areas extending for some thousands of square kilometers (up to 100 x 100 km), with a ground resolution of the order of 80 x 80 m [11]. The obtained products are particularly suited for regional scale displacement analysis, but can be conveniently used to outline individual and multiple distant sites affected by ground deformation. At local scale, with a ground resolution of the order of 10x10 m,[12] the technique leads to detection and analysis of local deformation that may affect single buildings.

6.2 Study area

The overall geological setting and morphology of the investigated area, which includes the metropolitan area and surroundings of Rome (Italy) (see figure 6.1)[23] are mainly the result of a sequence of alternated sedimentation and erosion cycles occurring since the upper Pliocene period and closely connected to tectonic evolution, volcanic activity and climate changes.

During the Pliocene period in this area, submerged by the Tyrrhenian Sea, a deposition process of silty and clayey soils, reaching a thickness of about 800 m, occurred. The deposits of the marine succession were involved in tectonic phases which induced the uplift (emersion) of the area and the formation of the Monte Mario-Gianicolo ridge. Moreover, this uplift also determined the formation of a fluvial-lacustrine and fluvial-marsh environment characterized by the presence of an important river, referred to as Paleotevere, which caused the deposition of wide and thick layers of alluvial deposits. The river bed was lately modified as a consequence of the tectonic process, which displaced the plio-pleistocenic substratum, and of the mean sea level variations related to the glaciations that occurred during the Quaternary period. Its evolution included both deviations from its original central axis and displacements of its mouth.

Subsequently, about 0.6-0.3 My ago, the volcanic activity

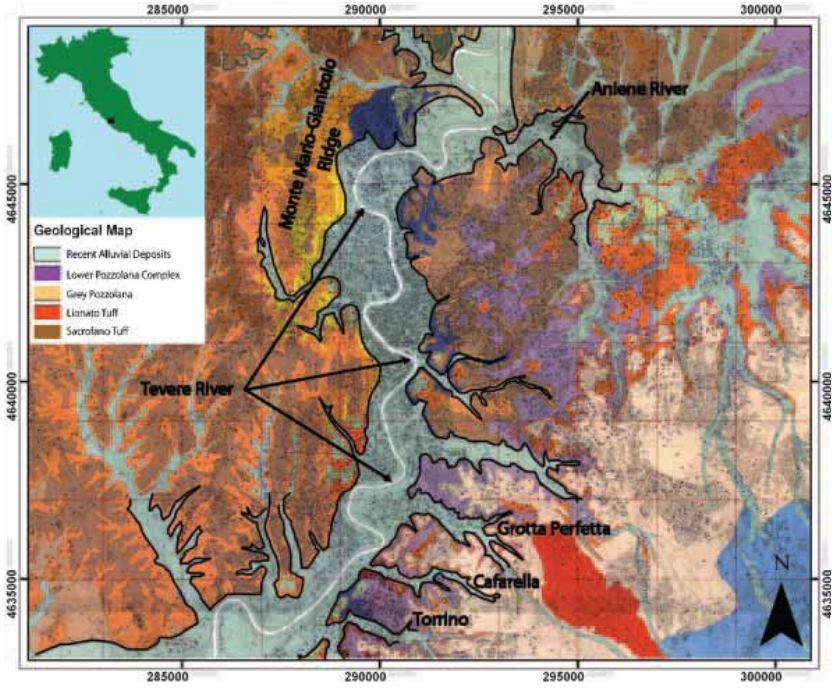

Figure 6. 1

Litho-stratigraphic map of the metropolitan area of Rome with the lithological limits of the major alluvial deposits formed by clays and silts sediments accumulated by the Tevere and the Aniene rivers highlighted.

strongly modified the morphology of the area with the deposition of a mantle of volcanic products (pyroclastics and lava) which obstructed and further modified the path of the Paleotevere. In particular, the accumulation of the volcanic products of the Alban Hills volcanic complex forced the river bed to turn toward the Monte Mario-Gianicolo ridge. During the last phase of the sea level lowering, corresponding to the last glaciation (Wurm), the river has deeply excavated its actual valley in the volcanic and sedimentary successions down to a level of 40 meters below the present mean sea level.

During the Holocene period, due to the raising of the mean sea level up to the present value, the progressive filling of the main valley occurred, thus producing the present alluvial plain that is limited by the Monte Mario-Gianicolo ridge to the West and by the shallow hills (the “Seven Hills” of Rome) forming the margin of the Alban Hills volcanic complex.

6.3 DInSAR analysis within the urban area of Roma

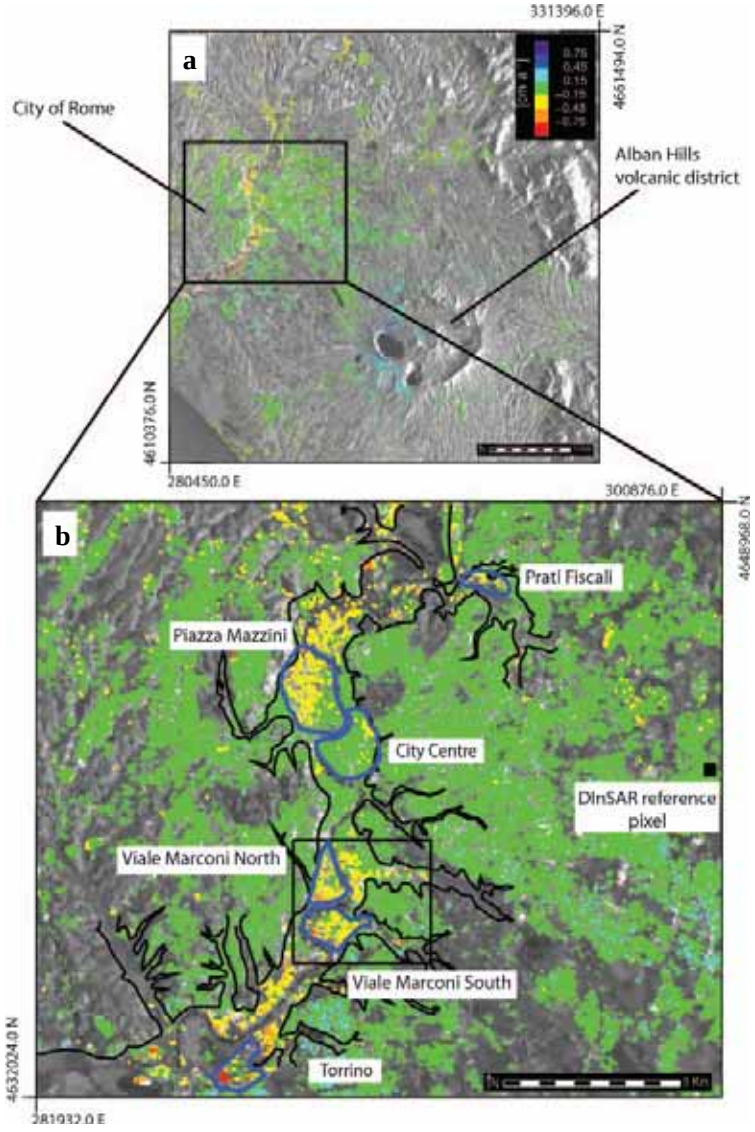

Figure 6. 2

Low-resolution differential synthetic aperture radar (SAR) interferometry (DInSAR) results. (a) Mean deformation velocity map of the investigated area superimposed on to a SAR amplitude image; (b) the highlighted zone, shown in the inset, is relevant to the metropolitan area of Rome with the map of the lithological limits of the major alluvial plain

6.3.1 Large scale deformation analysis

In order to investigate the deformation of the study area, the SBAS approach has been applied to a data set of 43 SAR images acquired by the ERS satellites on descending orbits (track 79, frame 2763), spanning the time interval from May 1995 up to June 2000. These images have been paired in 140 interferograms characterized by spatial and temporal baseline values smaller than 350 m and 4 years, respectively.[23]

The analysis is performed by considering the results of the large scale/low resolution data processing; in order to provide first an overall picture of the investigated area. In Figure 6.2a the estimated DInSAR mean deformation velocity map, geocoded and superimposed on a SAR amplitude image of the zone, is presented.

Several deformation effects can be identified in figure 6.2a. First of all, it is clearly visible the uplift phenomenon affecting the Alban Hills volcanic district, situated about 30 Km away from the southeastern side of the metropolitan area of Roma. Moreover, several subsiding zones, belonging to the urban area of Rome, are evident in figure 6.2a and, particularly, in the inset (figure 6.2b).

In order to investigate these subsidence phenomena, a comparison of DInSAR mean deformation velocity map of figure 6.2a with the geological map of the city of Rome [24] that is shown in figure 6.1, has been performed. Note that, in figures 6.2b, the simplified lithological limits of the alluvial deposits along the valleys of the Tevere and Aniene rivers is overlapped to the DInSAR map.

From the comparison of figures 6.1 and 6.2b it clearly appears that all the subsiding areas occur in correspondence of the alluvial plain of the Aniene and, above all, of the Tevere river and its tributaries; here the DInSAR-SBAS analysis provided negative velocities ranging from 1 mm/year to few peak values exceeding 1 cm/year.

The relationship between the measured settlements and the intrinsic characteristics as well as evolution of the recent alluvial deposits of the area, is now investigated.

The Holocene alluvial terrains are mainly formed by clayey silts and sandy silts and by silty sands with gravel lens. Generally, the fine-grained (cohesive) soils are of high plasticity and low consistency; the coarse-grained materials (sands and gravel) are loose or have low or medium relative density. Moreover, there are frequent lenses of organic materials and peat clay; as a consequence these deposits are highly compressible.

The overall thickness of these layers can reach 40-50 meters all over the urban area. The groundwater table in the alluvial deposits is located a few meters below the surface (5-10 meters) and the piezometric surface generally follows the hydrometric variations of the Tevere river. In some areas, perched groundwater tables are connected to the local stratigraphic conditions and fed by leakages from older aqueducts or sewers.

Another aspect that should be considered is that the urbanization of the alluvial plain has required, since the first century of the history of Rome, the raising of the original surface by means of antropic fills and embankments. These, initially, were emplaced to fill depressed marsh areas and to prevent their frequent inundations. The thickness of these layers locally varies and, in some cases, it can be more than tens of meters [25].

Overall, the observed displacements can be the result of a natural compaction or consolidation of the recent alluvial deposits which, as a consequence of their high compressibility, can be affected either by the variation of the groundwater table and/or by the action of overloads related to the urbanization.

Conversely, it should be observed that the subsiding areas correspond to a portion of the whole alluvial plain and are, in many cases, contiguous to zones apparently not affected by deformation. Such irregular distribution of the subsiding areas can be compared to the variation of the characteristics of the soils forming the alluvial deposit as well as to irregular and localized lowering of the water table level.

However, the ages of construction of the existing buildings located in areas urbanized in different periods (macroscopically homogeneous zones only were considered) were compared with the estimated DInSAR mean deformation velocity map. In particular, the magnitude of the displacements appears to decrease with the age of the buildings: for example, in the historical area of the city of Rome, where the antropic fills thicknesses are similar or even larger than those of other areas, no significant displacements were observed; on the contrary, in the most recently built up area around Viale Marconi (see figure 6.2b) significant deformations are visible.

Moreover, it should be also emphasized that the largest displacements were detected in correspondence of the minor tributaries located on the south-eastern side of the Tevere river; these areas, referred to as Viale Marconi north, Viale Marconi south and Torrino (see figure 6.2b), correspond to the Grotta Perfetta, Cafarella and Torrino valleys, respectively (see Figure 6.1). These valleys are characterized by mild slope angles which, during the Holocene period, established the conditions for the development of a marshy area and favored the deposition of silt-clay soils, including lenses of organic and highly compressible materials, which are less frequent on the opposite side of the river [24].

Accordingly, on a large scale interpretation, a major contribution to the deformation phenomena can be attributed to the different development stages of the consolidation process of the alluvial deposits, in presence of the overloads induced by the urbanization.

Moreover, the observed large scale displacement effects can be locally influenced by the peculiar terrain stratigraphical and lithological conditions. For instance, this is the case of the Piazza Mazzini area (see figure 6.2b) where the zone affected by the more significant deformation phenomena corresponds to a lens of peat clay [24].

Furthermore, the displacements of each building can be influenced by other effects, such as the building structural characteristics and the type of foundations. For example, deformation can be due to foundations not reaching the more rigid layers and whose piles float on shallower loose terrains [26] This is the case of

the Viale Marconi south zone, depicted in figure 6.2b, where significant buildings damages are reported [27]; a discussion on these effects is presented in the following sections.

6.3.2 Local scale deformation analysis

The capability of the SBAS approach to "zoom in" on selected areas and to detect and analyze deformation at the scale of a single building or man made structure is evident in Viale Marconi deforming

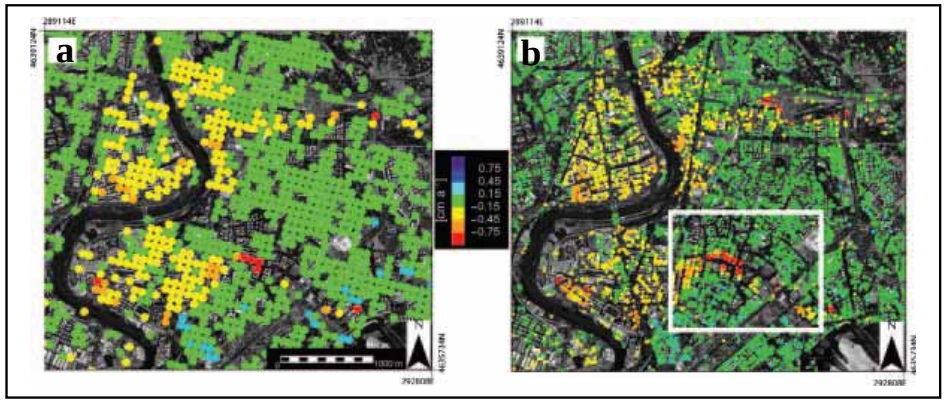

Figure 6. 3

Differential synthetic aperture radar (SAR) interferometry (DInSAR) results relevant to the Viale Marconi areas. (a) Low-resolution mean deformation velocity map superimposed on to an ortophoto of the investigated area; (b) full resolution mean deformation velocity map of the same area, with highlighted the zone investigated in figure 6.4 (white box).

areas, highlighted by the black box of figure 6.2b. This zone has been investigated by applying the SBAS procedure to the corresponding portion of the full resolution DInSAR interferograms.

The low and the full resolution DInSAR results, relevant to the investigated zone, are shown in figures 6.3a and 6.3b, respectively. By comparing these two maps, it is evident the improvement obtained by exploiting the fine resolution SAR data.

A detailed analysis and interpretation of the full resolution retrieved deformation has been conducted in this area. In particular, the analysis is concentrated on the zone relevant to a sector of the Grotta Perfetta area, corresponding to a minor lateral valley of the Tevere river (see figures 6.5a and 6.5b). The map shown in figure 6.5a combines the geological information on the investigated area with the SBAS results. The locations of two geological cross-sections obtained along and across the main direction of the valley [27] are also indicated on the map.

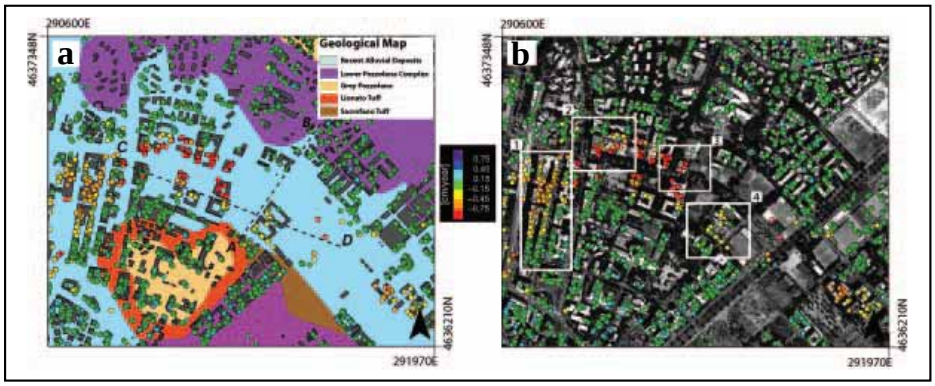

Figure 6. 4

Differential synthetic aperture radar (SAR) interferometry (DInSAR) results relevant to the Grotta Perfetta sector of the Viale Marconi South area.
(a) Simplified geological map of the zone with the full resolution mean deformation velocity map superimposed and with two geological cross-sections along the paths indicated by the dashed segments A–B and C–D, respectively; (b) full resolution mean deformation velocity map superimposed on to an ortophoto of the area with the four test areas labeled as 1, 2, 3 and 4 highlighted (white boxes).

The analysis of the cross-section C-D, shown in figure 6.5, give evidences to local variations of the stratigraphy along the valley: the thickness of the alluvial deposits reaches a maximum depth of 45 m towards the West (closer to the Tevere river bed) and becomes thinner on the eastern side; the cross-section A-B of figure 6.4a

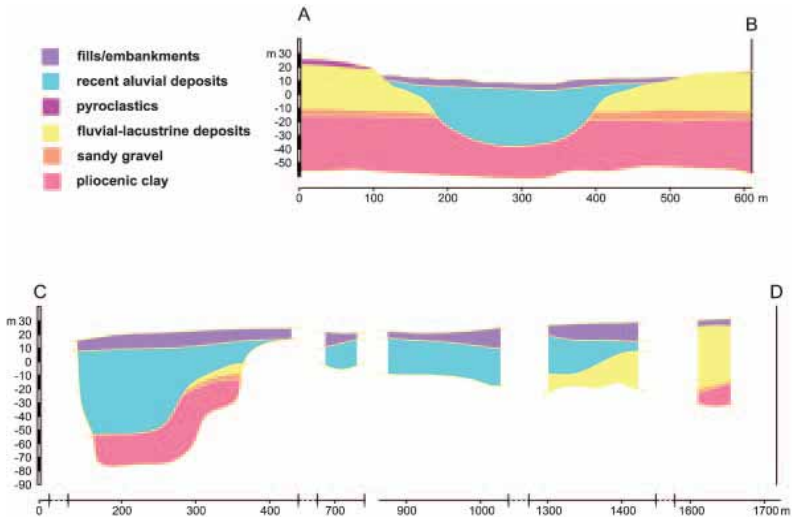

Figure 6. 5

Geological cross-sections of the alluvial deposits of the Tevere and Aniene rivers, corresponding to the A–B and the C–D dashed lines shown in figure 6.4(a).

depicts the situation across the valley and allows to infer the form of the depression filled by alluvial deposits which corresponds to the main axis of the valley. Note also that the fills and the embankments are differently distributed in the area, though they were generally placed in order to increase the elevation from about 10 to 15 m a.s.l.. The soil in this area is formed by alluvial Holocene deposits. Moreover, geotechnical analysis demonstrated that the alluvial deposits are highly compressible and under consolidation due to the presence of clays and silts.

The urbanization of this area was completed between 1949 and 1970: in the first decade most of the fills and embankments were emplaced while the majority of buildings were completed between

1950 and 1960. Most buildings are composed of different structures connected by dilatation joints and are generally founded on piles of a length ranging from 15 to 20 m, with 1-2 underground floors.

Owing to the occurrence of major deformation phenomena observed on many buildings, a number of studies [27] [28] devoted to structural monitoring and terrain characterization were carried out in this area. Monitoring activities included topographic observation of vertical misalignments of external walls and vertical displacement observation, by levelling surveys. Though the collected data were not extended to the whole area and do not cover a long period of observation, they contributed to evaluating the stability conditions of a few buildings resulting in either their consolidation or even demolition for the most damaged ones.

The quantitative and qualitative analyses conducted on the area

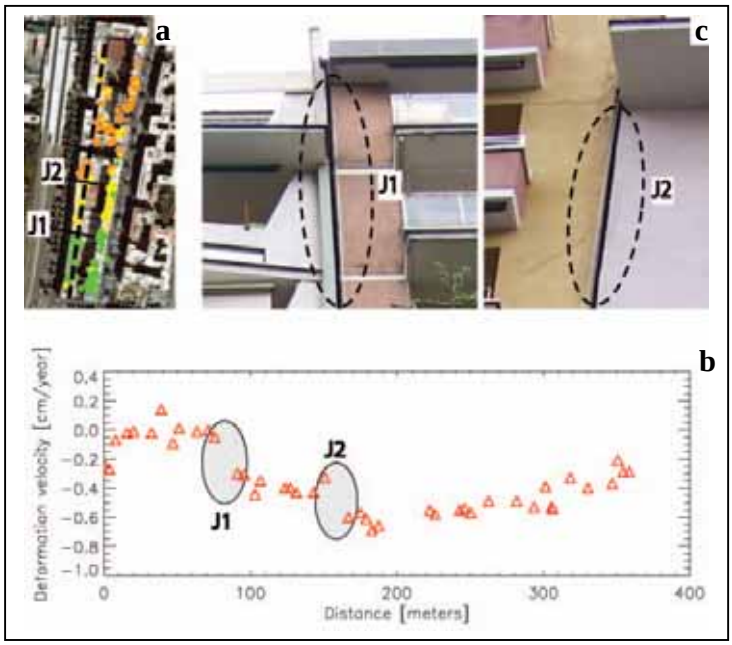

Figure 6. 6

Results relevant to area 1 in figure 6.4(b). (a) Optical image of the alignment of the buildings with the full resolution differential synthetic aperture radar (SAR) interferometry (DInSAR) mean deformation velocity map superimposed; (b) plot of the cross-section (dashed segment in (a)) of the measured mean deformation velocities. The two discontinuities occurring in correspondence with points J1 and J2, corresponding to the sites shown in the two figures of inset (c).

well agree with the interpretation that most damaged buildings have foundations which do not reach the deeper and more rigid soils (plio-pleistocenic layer) but are partly, or completely, founded on poor soils represented by alluvial deposits. In this situation, the bearing capacity of foundations can rely only on the lateral resistance of piles but not on their cap resistance, resulting in translational and rotational (not necessarily rigid) movements [28].

The analysis of the SBAS velocity map in figures 6.5A and 7.5B allows to more clearly highlight the relationship between the position of the buildings and the magnitude of the observed deformation: larger deformation velocities are measured along the central axis and the western side of the valley, where the alluvial deposits are thicker; moreover, the velocities decrease moving away

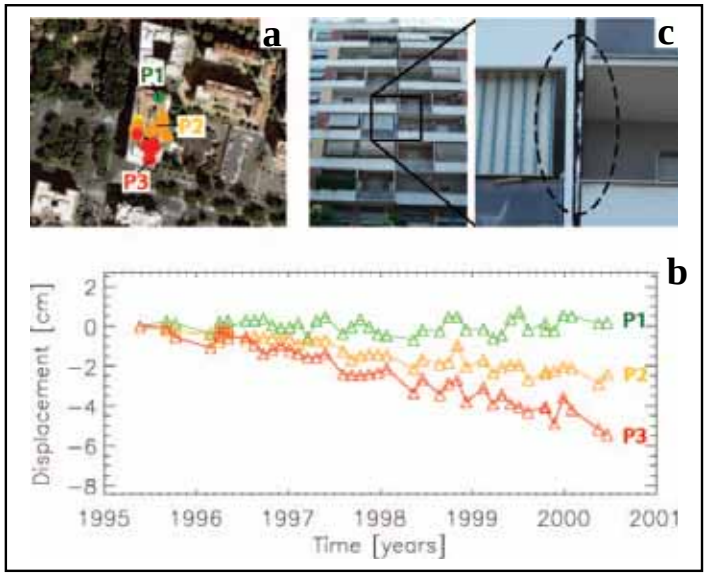

Figure 6. 7

Results relevant to area 2 in figure 6.4b). (a) Optical image of the investigated building with the full resolution differential synthetic aperture radar (SAR) interferometry (DInSAR) mean deformation velocity map superimposed; (b) deformation time series relevant to the pixels labeled P1, P2 and P3, respectively in (a). Evidence of the detected deformation phenomenon is revealed by the image of the building shown in inset (c).

from the valley central axis and are very low in an area toward east

where no fills are present. This effect is particularly evident in the alignment of buildings labelled as 1 in figure 6.4b and zoomed in Figure 6.6a.

In this case it is clear the presence of a deformation spatial gradient that is affecting the overall structure. To quantitatively investigate this effect, in the plot of figure 6.6b, a cross-section of the measured mean deformation velocities is presented. The two discontinuities occurring in correspondence of the points J1 and J2; correspond to the sites shown in the inset of figure 6.6c, characterized by a significant displacement revealed on the buildings dilatation joints.

Moreover the SBAS results allow providing information not only on the spatial characteristics but also on the temporal evolution of the deformation affecting a large number of buildings that are present in the area. In order to stress this deformation analysis capability, some key examples are shown in the following.

First the building, labelled as 2 in figure 6.4B and highlighted in the zoom, shown in figure 6.7a is considered. In this case, a very significant deformation appears in the DInSAR map; this effect is even more evident in the comparison of the deformation time series relevant to the pixels labelled in figure 6.7a as P1, P2 and P3, respectively (see the plots of figure 6.7b). Note that an overall differential deformation of about 1 cm/year has been detected between the pixels P1 and P3 whose distance is of about 55 m. The evidence of this deformation phenomenon is again revealed by in situ inspection, as testified by the picture of the building shown in the inset of figure 6.7c.

As additional examples, the buildings labeled in figure 6.4b as 3 and 4 that have been highlighted in the zooms shown in Figure 6.8a and Figure 6.9a, respectively. These two sites are particularly relevant because some leveling measurements have been carried out and have been made available.

Accordingly, the retrieved DInSAR displacements with those available from the leveling measurements are compared. In this case a vertical displacement effect and the projection of the leveling data along the SAR sensor LOS, in order to make them comparable with the SAR measurements, is assumed. Moreover, in order to have a

common reference point for the data shown in figure 6.8a, the DInSAR deformation time series have been recomputed with respect to the pixel marked as P2; in addition, the benchmark L2, that is the closest one to the pixel P2, as reference for the leveling measurements is assumed,. This operation was also repeated for the data shown in figure 6.9a where, again, the SAR pixel labeled as P2 and the corresponding leveling benchmark L2, have been considered as

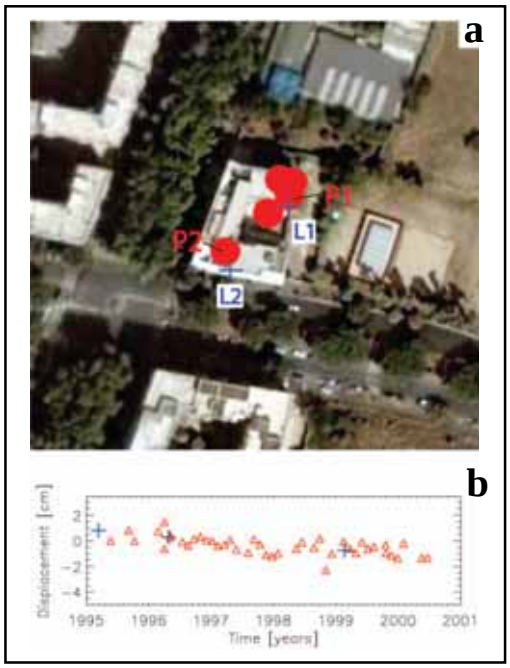

Figure 6. 8

Results relevant to area 3 in figure 6.4(b). (a) Optical image of the investigated building with the full resolution differential synthetic aperture radar (SAR) interferometry (DInSAR) mean deformation velocity map superimposed; (b) comparison between the time series relevant to the DInSAR displacements (red triangles) of the SAR pixel P1 and of the corresponding line-of-sight (LOS) projected leveling measurements (‘ + ’ symbol) of the benchmark L1.

reference points.

In particular, in Figure 6.9b the comparison between the deformation time series of the SAR pixel P1 (red triangles) and the

leveling measurements of the corresponding benchmark marked as L1 is presented. By considering the DInSAR deformation time series shown in the plot of figure 6.8b, a rather linear differential displacement of about 3 mm/year between the pixels P1 and P2 is measured; this deformation trend is fully confirmed by the leveling data.

For what concerns the site of figure 6.9a, the DInSAR

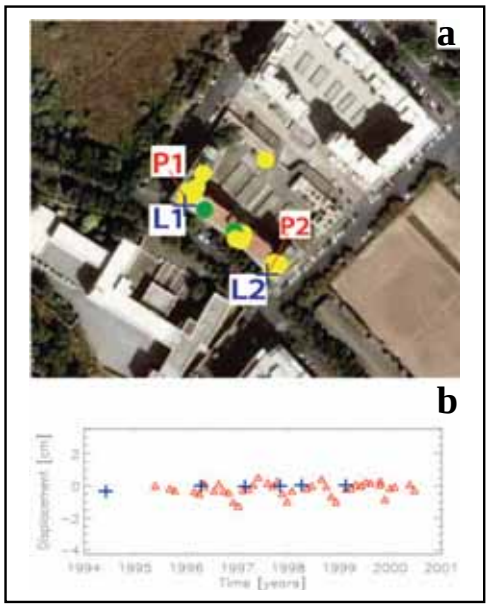

Figure 6. 9

Results relevant to area 4 in figure 6.4(b). (a) Optical image of the investigated building with the full resolution DInSAR mean deformation velocity map superimposed; (b) comparison between the time series relevant to the DInSAR displacements (red triangles) of SAR pixel P1 and of the corresponding LOS-projected leveling measurements (‘ + ’ symbol) of the benchmark L1.

deformation time series of the pixel P1 (see figure 6.9b) shows nearly no deformation signal with respect to P2; also in this case the result is confirmed by the levelling data.

Moreover, the DInSAR measurements exhibit an oscillation behavior that is very likely related to thermal dilatation phenomena.

6.4 Summary

In this chapter a successful application of the two-scale surface deformation retrieval approach based on SBAS technique, has been presented. This analysis, focused on an ERS 1-2 SAR data set relevant to the city of Rome (Italy), has clearly shown that the low resolution SBAS-DInSAR processing is a valuable tool for large scale deformation survey of the investigated areas. Indeed, significant information on the spatial and temporal characteristics of the detected deformation can be retrieved.

In this case, the carried out analysis allowed detecting and analyzing numerous subsidence phenomena affecting the urban area of the city of Rome and its surroundings. Moreover, the full resolution DInSAR data demonstrated the capability of the approach to provide information about localized deformation phenomena at the scale of single buildings. In particular, a key issue of the presented analysis is the evidence that differential deformation of buildings, of few mm/year, can be detected; this allows the identification of structures that may be potentially involved in critical situations.

Finally, an interpretation of the detected phenomena, addressing the different development stages of the consolidation process of the alluvial deposits, due to the overloads induced by the urbanization, as a key contribution to the revealed displacements, has been provided.

Chapter 7

Ground Deformation Detected Using the Two Scales SBAS-DInSAR Technique in the Umbria Region

7.1 Introduction

This chapter will address the analysis, at two scale spatial resolution, of ground deformation affecting the Umbria region (central Italy).In particular, low-resolution deformation maps are used to identify and measure subsidence induced by exploitation of a confined aquifer in the Valle Umbra; the full-resolution deformation maps are used to investigate the movement of the Ivancich landslide, in the Assisi Municipality.

7.2 Study area

The study area extends for about 7500 km^2 in Umbria, central Italy, with elevations ranging from 48 m along the Nera River flood plain to 1684 m at M. Coscerno. In this area, the landscape is hilly or mountainous, with large open valleys and intra mountain basins drained by the Tiber River and its tributaries (Figure 7.1). In the area, sedimentary rocks, pertaining to the Umbria-Marche stratigraphic sequence, Lias to Eocene in age, overlaid by lake deposits, lower Pliocene to Quaternary in age, and by fluvial deposits of Recent age [29] [30], crop out. The lake and fluvial deposits host deep-seated and shallow aquifers exploited chiefly for human and agricultural uses.

The structural setting is complex, and results from the superposition of

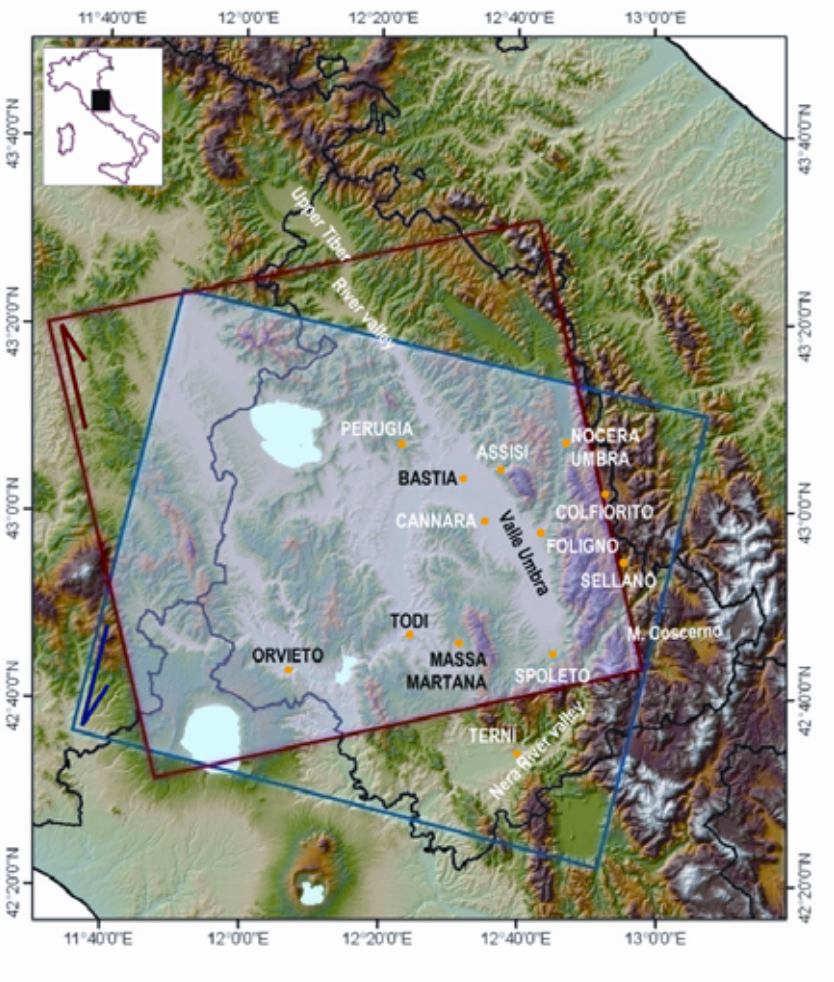

Figure 7. 1

Map showing terrain morphology in Umbria, central Italy. Inset shows approximate location of study area. Red box shows extent of ERS-1/2 footprint for track 172, frame 855 (ascending orbit). Blue box shows footprint for track 351, frame 2745 (descending orbit).

two tectonic phases associated to the formation of the Apennines mountain chain. Due to the geological and climatic settings, landslides are abundant in Umbria and contribute to shape the landscape [37] [38]. More than 93% of the region is covered by vegetation, including 41% forest, 10% grassland, and 42% cultivated areas.

7.3 DInSAR analysis

Starting from a large set of ERS-1/2 acquisitions along the satellites descending orbit (track 351, frame 2745), 49 images in the

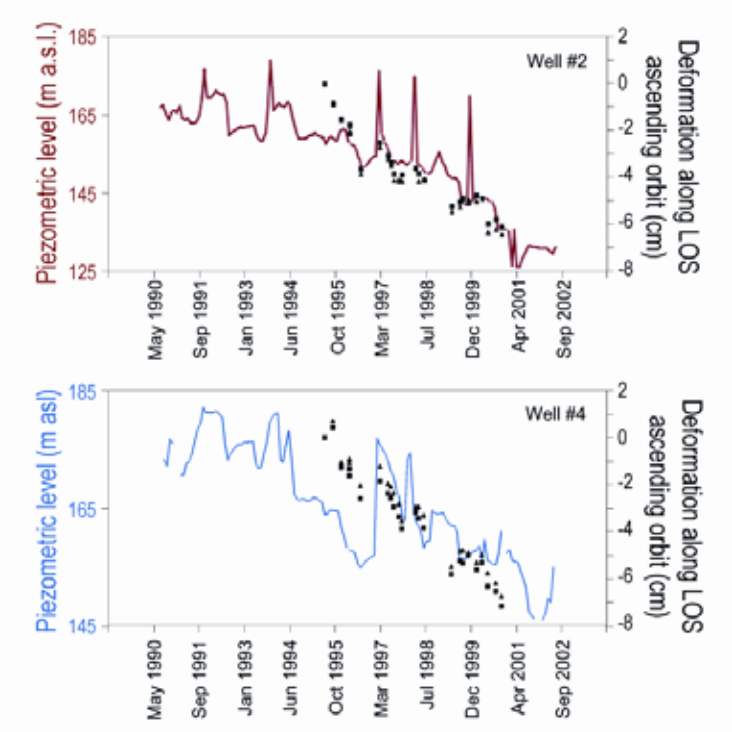

Figure 7. 2

Cannara well field. Comparison between the temporal pattern of the piezometric surface (lines) and deformation of points on the topographic surface located within a distance of 200 m from the wells (symbols). Deformation measured along the satellites LOS (descending orbit).

period from April 1992 to December 2000 were singled out and 124 interferograms were computed. Similarly, from the available set of acquisitions along the satellites ascending orbit (track 172, frame 855), 24 images in the period between June 1995 and November 2000 were selected, and 67 interferograms were computed. [33]

First, from the ascending and the descending ERS-1/2 image dataset, the standard SBAS approach was used to obtain low-

resolution, mean deformation velocity maps. Next, the advanced

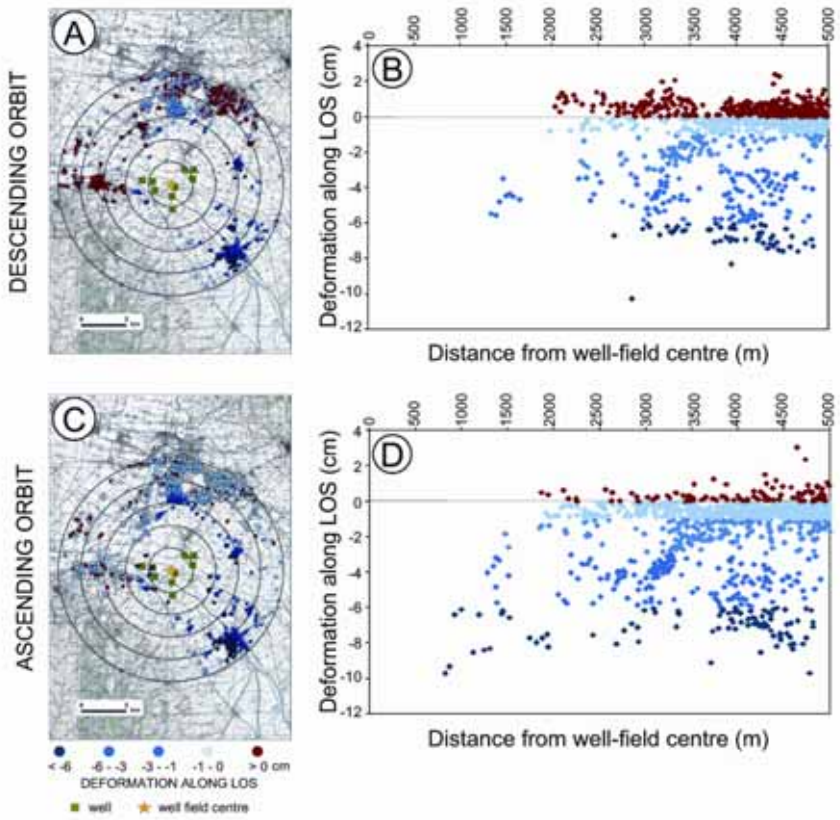

Figure 7. 3

Geographical pattern of the surface deformation detected through the SBAS-DInSAR technique in the area surrounding the Cannara well field. (A) and (C) show geographical pattern of the LOS deformation measured along descending and ascending orbits, respectively. (B) and (D) show relationship between detected deformation and distance to the well field centre (star), for descending and ascending orbits, respectively.

SBAS technique was used to determine full-resolution, mean deformation velocity maps for selected areas.

7.3.1 Deformation induced by aquifer exploitation

In the Umbria region, the low resolution ground deformation maps for the period 1995-2000 obtained through the SBAS-DInSAR

technique show subsidence of a portion of the Valle Umbra south of Assisi and west of Foligno. Where subsidence is largest (i.e., near the village of Cannara; Figure 7.1), a field of nine wells extracts water from a deep, confined aquifer.

It is of interest to analyze the temporal and the geographical relationships between variations of the piezometric surface and ground deformation in the zone of influence of the well field. Figure 7.2 shows, for two representative wells (#2 and #4), a comparison between the temporal pattern of the piezometric surface (lines) and the displacement of surface points located within a distance of 200 m from the wells (symbols). Deformation was measured along the satellites LOS. The deformation patterns for the ascending and the descending orbits are similar, indicating that displacement was mostly vertical. This was expected; given water withdrawal was the mechanism driving the deformation.

Analysis of the spatial pattern of the retrieved deformation (Figure 7.3) allows for the following considerations. Deformation was largest near the centre of the well field, and decreased with increasing distance from the wells. The largest shown deformation in the 5.5-year period exceeded, on average, 5 cm (at a distance of about 1000 m), corresponding to an average deformation of 0.9 cm·yr-1. Deformation was undetectable (i.e., was within the DInSAR measurement error) for distances exceeding 2000 – 3000 m from the well field centre. This is in agreement with the hydrologic and geometric characteristics of the examined aquifer, and the known pumping rates [34]

DInSAR deformation pixels are not available in an area between a few meters to ≈ 500 m from the wells. Objects that scatter the radar signal are present in this area, including buildings and roads.

Lack of coherent pixels is taken as indication of significant – and occasionally rapid – ground deformation that resulted in loss of coherence of the scattering points. As a final issue, a distinct cloud of points with deformation in the range from -3 to -10 cm is present at a distance between 3500 and 5000 m from the wells (Figure 7.3 B,D), in correspondence to the Cannara village (Figure 7.3 A,C). The pattern of deformation shown in this area is not in agreement with the presence and location of the cone of influence induced by the well field (i.e., the measured deformation is too large given the distance from the wells). Hypotheses to explain the observed deformation include: (i) significant heterogeneities in the aquifer geometry (e.g., the presence of a low permeability barrier bounding the aquifer to the

S) or lithology (e.g., the presence of compactable lake and fluvial deposits), and/or (ii) additional water withdrawal centered on or near the Cannara village.

7.3.2 SBAS-DInSAR low resolution analysis to detect and monitor landslides in Umbria Region

To analyse the performance of the SBAS-DInSAR technique to detect and monitor landslides in Umbria, the available landslide inventory map (Figure 7.4A) was intersected in a GIS with the low-resolution DInSAR deformation maps. The geographical operation

	Area	Number of Landslides				Landslide Area			
		Total		Intersection		Total		Intersection	
	Km^2	#		#	%	km^2		km^2	%
Track 351, Frame 2745 (descending orbit)	6504	33,500	(A)	919	2.7	506.3	(A)	52.8	10.4
			(B)	312	0.9		(B)	41.7	8.2
Track 172, Frame 855 (ascending orbit)	6218	33,461	(A)	1148	3.4	541.6	(A)	69.5	12.8
			(B)	396	1.2		(B)	49.0	9.1
Area common to the two frames	5226	26,398	(A)	149	0.6	405.5	(A)	11.6	2.9
			(B)	44	0.2		(B)	9.4	2.3

Table 7. 1

Number of landslides and extent of landslide area that contains DInSAR information in the examined area. (A) Data computed considering extent of DInSAR pixels, approximately 80 m × 80 m in size. (B) Data computed considering the centre of DInSAR pixels.

allowed for the calculation of the total number of landslides and the total landslide area that can be potentially monitored using the available data and the adopted technology (Table 7.1). Two tests were performed.

In the first test (test #1), the SAR data were transformed to a regular grid with a ground resolution of 80 m × 80 m. The gridded data were then transformed into polygons (squares) and intersected with the landslide inventory map. In the second test (test #2), the individual SAR pixels were considered as points (located in the pixel centre), and landslides containing individual or multiple SAR points were identified. The two tests were performed considering the deformation measured along the satellite ascending and descending orbits (LOS deformation), and the E-W and vertical deformation

components computed where both ascending and descending orbits data were available.

Results of the two tests are listed in Table 7.1. The percentage of the mapped landslides that contains at least one coherent SAR point

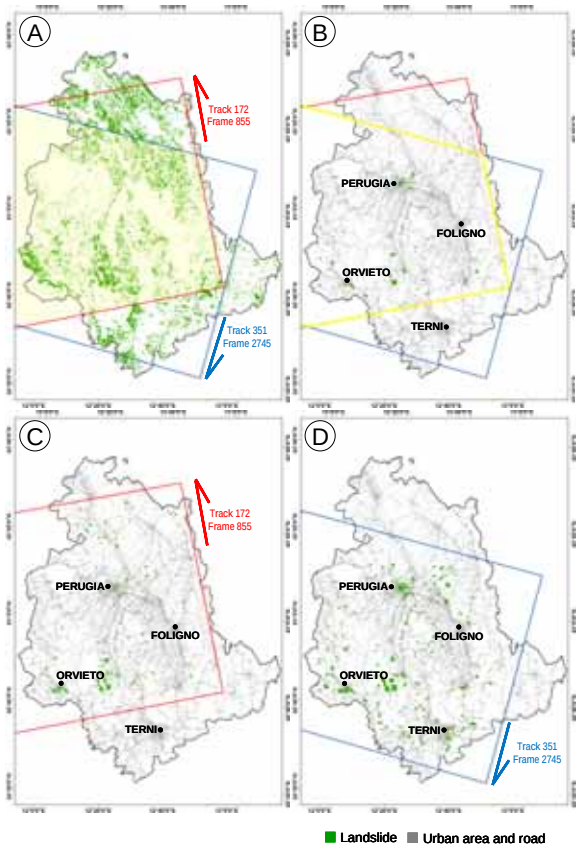

Figure 7. 4

Geographical distribution of known landslides in Umbria. (A) Landslide inventory map (B) Landslides where both ascending and descending orbit SAR data are available and for which the vertical and the E-W deformation components can be monitored. (C) Portion of the inventory showing landslides that can be monitored by applying the SBAS-DInSAR technique to the data relevant to track 172, frame 855 along the ERS-1/2 ascending orbit. (D) Similar to (B), using track 351, frame 2745 along the ERS-1/2 descending orbit.

(test #2) is 0.9% for the ascending orbit (Figure 7.4C) and 1.2% for the descending orbit (Figure 7.4D). The percentage reduces to 0.2% (44 landslides, Figure 7.4B) where data are available from both the

ascending and descending orbits and the vertical and E-W surface deformation components can be measured using the adopted SBAS-DInSAR technique. The percentage of landslide area that can be monitored is largest for the ascending orbit (9.1%, Figure 7.4C), is slightly reduced (8.2%) for the descending orbit (Figure 7.4D), and is significantly reduced (2.3%) where both orbits are considered (Figure 7.4B). When the gridded SAR data are considered (test #1), the proportion of landslides with relevant deformation data increases to 2.7% for the ascending orbit, to 3.4% for the descending orbit, and is 0.6% (149 landslides) where both the orbits are considered. Correspondingly, the proportion of landslide area that can be monitored is 10.4% for the descending orbit, 12.8% for the ascending orbit, and reduces to 2.9% where the two orbits are jointly considered.

Visual examination of Figure 7.4 reveals that, where SAR information is available, landslides are located in urban areas or along roads (e.g., Perugia, Assisi, Orvieto), or are particularly large mass movements (e.g., slides W of Todi). The different percentages of landslides and of landslide areas identified by the two tests (Table 7.1) are a consequence of the different GIS strategies adopted for the analysis. Test #1 overestimates the detected landslides, because it considers (erroneously) a small landslide located near or at the boundary of a SAR pixel as containing relevant SAR information that – in reality – may be not present in the landslide. Conversely, test #2 underestimates the number of landslides; in places, the inventory map shows small (younger) landslides inside large (older) landslides. Where individual SAR points fall inside nested landslides, only the youngest (smallest) one is considered. Figures shown in Table 7.1 provide a range for the number and the area extent of the landslides that can be studied using the low-resolution SBAS-DInSAR approach and the available ERS 1/2 data in Umbria.

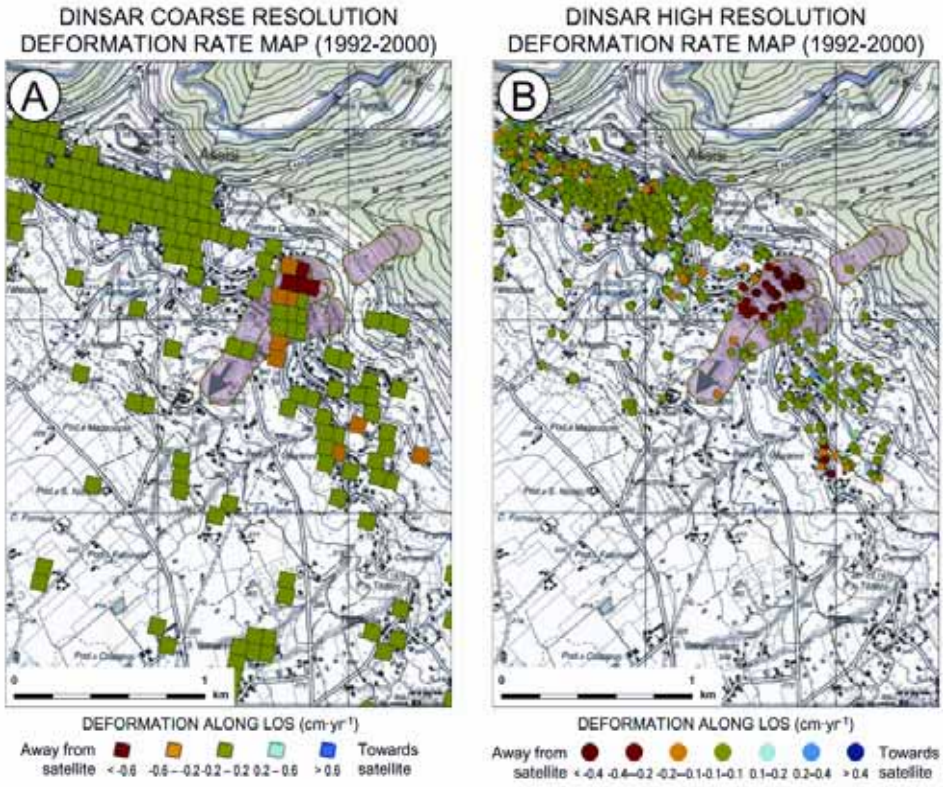

Figure 7. 5

Surface deformation maps for the Ivancich area, Assisi Municipality. (A) Low resolution deformation rate map (descending orbit). Gray arrow shows landslide main direction of motion. (B) Full resolution deformation rate map (descending orbit)

7.3.3 SBAS-DInSAR low and full-resolution analysis in the Ivancich landslide area

Multi-temporal SAR interferometry was already applied to detect and monitor landslides from space [35] [36] [37] [38]. Given the wavelength of most of the available space borne SAR sensors (mainly C band, about 5.6 cm) and the considerable repeat cycle of the acquisitions (27 to 35 days), only slow to very slow moving landslides

can be monitored. This limits the use DInSAR technology to study landslides.

In this case the SBAS-DInSAR analysis was performed in the Ivancich area, in Assisi Municipality (Figure 7.1). For this area, the coarse- and the full-resolution surface deformation maps (Figure 7.5) were used to investigate a slow moving, deep-seated landslide of the slide type that extends for about 3×10^5 m^2 in the area [39]. Movement of the landslide has caused repeated damage to roads, buildings, and retaining structures [40].

In the period from April 1992 to December 2000 (Figure

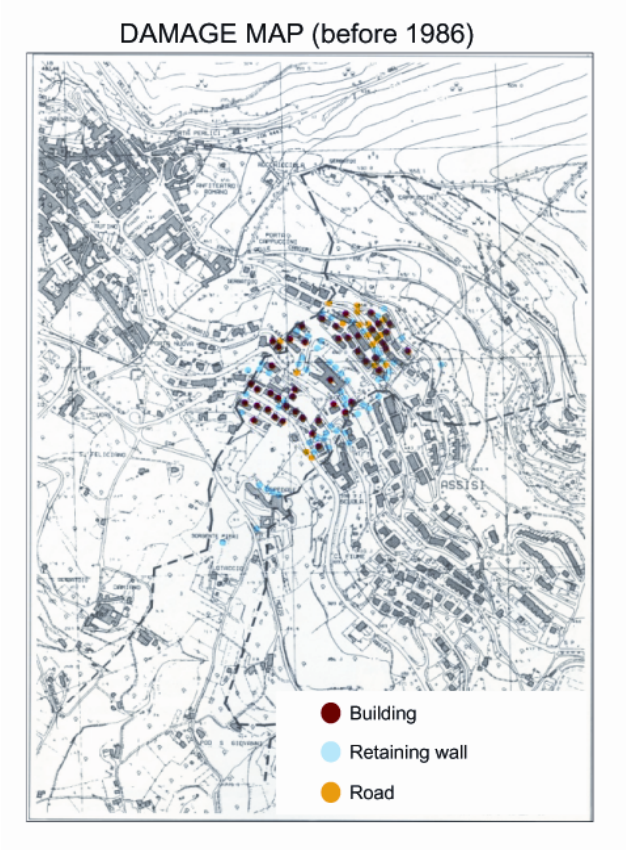

Figure 7. 6

Map showing damage to buildings, roads, and retaining structures

7.5A), a good agreement exists between the location of the landslide and the position of coarse-resolution SAR pixels that moved away

from the satellite descending orbit. The full-resolution SAR data (Figure 7.5B) confirm the spatial pattern of the ground deformation, and allow for the identification of a specific sector of the landslide that was more active during the investigated period, and the precise location of the boundaries of the most active landslide area. The pattern of deformation is in good agreement with the location of buildings, roads, and retaining walls that suffered damage in the Ivancich zone [45](Figure 7.6). Most of the damaged structures are located in areas where the deformation detected by DInSAR technology was large or very large (> 4 cm). This was expected, given the type of buildings present in the area (concrete-frame and brick-wall buildings) and the type of landslide.

The temporal pattern of the measured ground deformation in the landslide area, for the period between April 1992 and December 2000 is shown in Figure 7.7.

The deformation time-series analysis allows for the following considerations:

- the deformation was largest in the upper part of the failed slope, near the landslide crown area,
- the deformation was less intense in the central part of the active landslide area, and reduced further down the slope,
- the rate of deformation for the most active area remained about constant for most of the observation period, regardless of seasonal climate variations and changing meteorological conditions,
- the movement of the central and the lower parts of the landslide active area started several months after the onset of the (measured) deformation in the upper part of the landslide. The latter may reflect changes in the landslide deep-seated geometry and deformation pattern.

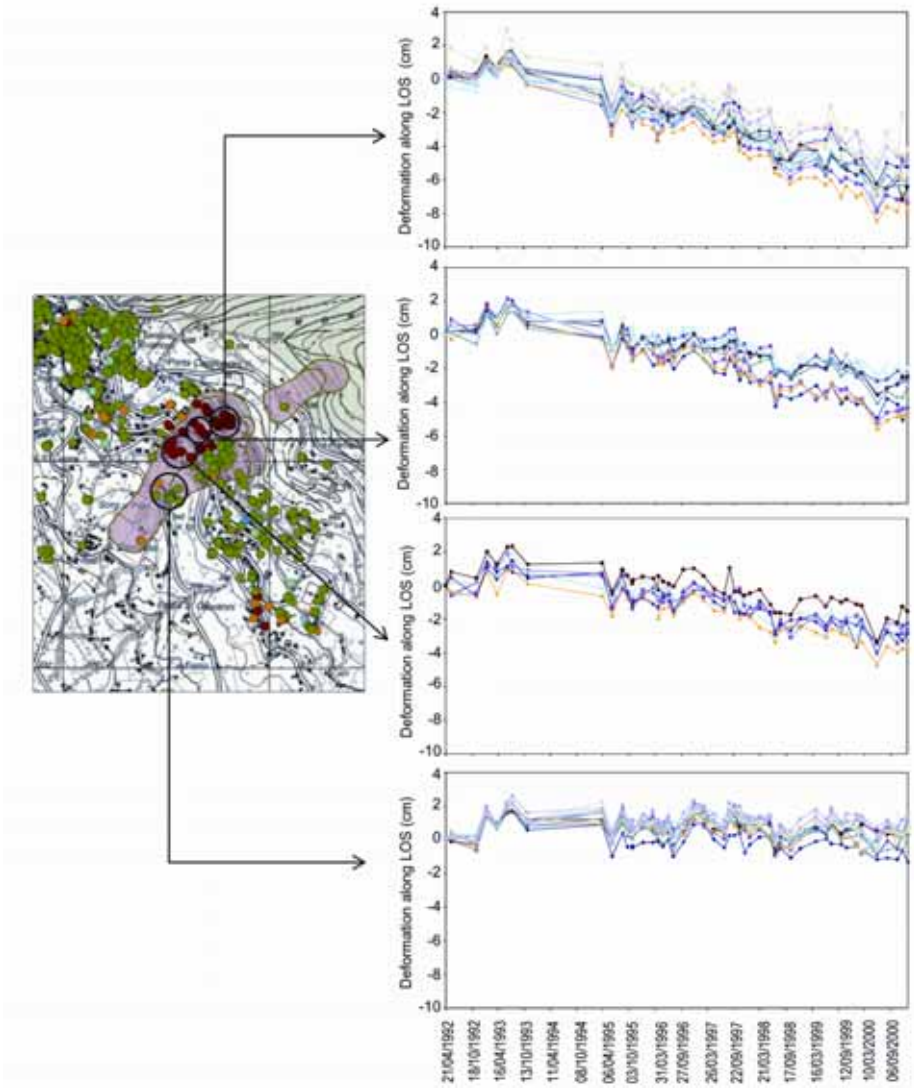

Figure 7. 7

Temporal pattern of the topographic deformation measured through the SBAS-DInSAR technique in the Ivancich area, Assisi Municipality. Deformation along LOS shown in cm for four areas in the landslide deposit.

7.4 Summary

To detect and analyze ground deformation in Umbria, central Italy, seventy-three SAR images acquired by the European Remote Sensing (ERS-1/2) satellites along ascending and descending orbits, in the period from 21 April 1992 to 29 December 2000, were used.

The low-resolution deformation maps, obtained by applying the SBAS technique has allowed identifying an area of active subsidence in the Valle Umbra, between Bastia and Cannara. In the area, a field of nine wells extracts water from a deep, confined aquifer. A relationship was determined between the time and the amount of the detected surface deformation and the quantity of the extracted water, suggesting a dependency of the ground deformation on the withdrawal.

Subsequently, to analyse the performance of the SBAS-DInSAR technique to detect and monitor landslides in Umbria, the percentages of landslides and of landslide areas were identified .These results reveal that landslides containing SAR information are located mainly in urban areas and along roads, or are particularly large mass movements. This was expected, given the characteristics of the exploited SAR sensor.

Finally, in the Assisi Municipality, movement of the Ivancich landslide was investigated exploiting the full-resolution SBAS-DInSAR data. The obtained full-resolution mean deformation velocity maps allowed singling out a sector of the landslide that was most active in the investigated period. Interestingly, the rate of deformation for the most active landslide area was found nearly constant during the observation period, despite considerable meteorological (rainfall) variations.

Concluding Remarks

This PhD Thesis has been focused on the exploitation of advanced DInSAR techniques to develop analyses on subsidence and slow-moving landslide phenomena at different spatial scales.

The thesis started from DInSAR basics (see Chapters 1-2) with special regard to the adopted multi-pass algorithms, referred to as Small BAseline Subset (SBAS) approach, and the key point of this work has been the application of the technique to the subsidence phenomena, ground deformation and landslide monitoring. The thesis has taken into account the different levels of details required by each study scale and the DInSAR data resolution.

With reference to subsidence phenomena both high- and low-resolution DInSAR data, obtained via SBAS algorithms, were validated and interpreted stressing their valuable use at regional, municipal or “at single building” scales.

In particular, DInSAR mean deformation velocity maps analysis allowed to detect an unknown ground deformation effect which involves the urban area of Satriano di Lucania, located close to Potenza, where three main deforming areas have been identified. In addition the temporal evolution analysis of the well-known gravitational phenomena affecting the Maratea valley, revealed the presence of temporal changes in the velocity of the landslide movements.

Referring to Sarno urban area (Campania Region, Italy) SBAS DInSAR data analysis was carried out at municipal scale. In this area several damages to buildings were recorded in the early ‘90s, due to subsidence-induced settlements related to huge water withdrawals.

The previous studies as well as the availability of topographic leveling measurements allowed the validation of low-resolution DInSAR data (derived by SBAS algorithm), highlighting a good matching in either point-wise comparisons or exhibited areal trend. This latter was also confirmed by the concentration of most deformable peat layers just within the zone where the highest settlements were recorded. Then, the gradient settlement map was

computed and compared with the localization of damages, mainly relative to masonry buildings with shallow foundations.

Subsequently, an analysis focused on an ERS data set relevant to the city of Rome (Italy),was performed. In this case, the two spatial scale analysis allowed to detect and analyze numerous subsidence phenomena affecting the urban area of the city of Rome and its surroundings. A detailed interpretation of the low and full resolution retrieved deformation has been conducted in these areas.

Finally, a two scale resolution, ground deformation analysis in the Umbria region (central Italy) were carried out. First, from an ascending and descending ERS-1/2 image dataset, the standard SBAS approach was used to obtain low-resolution, mean deformation velocity maps. Next, the advanced SBAS technique was applied for selected areas. In particular low-resolution deformation maps were used to identify and measure subsidence induced by exploitation of a confined aquifer in the Valle Umbra; to analyse the performance of the SBAS-DInSAR technique to detect and monitor landslides in Umbria; the full-resolution ones were used to investigate the movement of the Ivancich landslide, in the Assisi Municipality.

In conclusion, the obtained results showed that the use of SBAS-DInSAR approach can provide a useful contribution to the landslide and subsidence-related risk management process. A key element is certainly represented by the capability of the approach to provide information on the space-time characteristics of the detected deformation. More specifically, the availability of measurements relevant to the mean deformation (for instance, the mean deformation velocity patterns) with significantly extended spatial coverage, allows to identify peculiar features and to implement advanced post-processing operations; they may include, for example, the combination of the information retrieved from multiple radar LOS observations, finally leading to retrieve different components of the detected displacements.

Moreover, the capability of the SBAS technique to produce deformation time series represents another element of key importance because it leads to the detection of signal patterns that yield additional insight into the investigated signal process.

Regarding the main limitations of the SBAS technique, we can say that the phase unwrapping errors and the unfiltered atmospheric phase artifacts represent the main error sources in the deformation retrieval process; indeed, they may affect the accuracy and also the

coherent pixel density of the obtained results; the development of advanced techniques for improving the performances of the available algorithms is still an open research topic.

In addition to these critical issues there are also limitations related to the actual DInSAR technology that is essentially based on SAR sensors operating at C-band. In this case, as discussed and clearly shown in the results presented in this PhD thesis, the coherence is essentially maintained only in urbanized and rocky areas. In this context a key role can be played by the next generation sensors like the Japanese ALOS-PALSAR [5] system, that will operate at lower frequencies of the electromagnetic spectrum and in particular within the L-band. In this case, although a sensitivity reduction in the displacement detection will be caused by the wavelength increase, a significant improvement of the coherence characteristics is also expected in the generated DInSAR interferograms.

Another promising element is represented by the development of SAR sensor constellations such as the COSMO-SKYMED system [41] that should allow a significant reduction in the SAR sensor revisit time with a drastic, positive impact on the temporal decorrelation phenomena and would allow monitoring roughly four times faster surface deformations.

Of course, the advantage of using this technique is further emphasized in studies over large areas and this PhD Thesis represents one of the first examples of extensive use of DInSAR technology devoted to the subsidence phenomena and hydrogeological instability analysis.

The analyses developed in this work are, so, particularly appealing for activities dealing with land management. Indeed, the increasing interest in DInSAR technique is also testified, for instance, by the Piano Straordinario di Telerilevamento of Italian Ministry of Environment (2007), which chose DInSAR techniques as privileged tools for updating all thematic maps relevant to natural hazards such as: landslides, flood, subsidence, etc. In particular, concerning the DInSAR data, an image dataset with total coverage of the Italian territory will be available, thus posing the challenge of analyzing and properly interpreting such a huge amount of data.

Nevertheless, it should be emphasized that DInSAR technique is relatively new and its application to ground displacement monitoring is not standardized yet.

For this reason, particular attention will be devoted to achieve further improvement of both processing algorithms and validation/interpretation procedures.

Overall, future scenarios involving multi-frequency and multi-LOS SAR observation, coupled with reduced revisit time options, seem extremely promising for the development of advanced applications of the SBAS methodology and more generally for the DInSAR techniques. This may finally lead to the use of the DInSAR methodologies as part of routine surveillance scenarios.

References

[1] C. A. Wiley: “Pulsed Doppler radar methods and apparatus”, U.S. Patent 3,196,436, filed in 1954;

[2] S. H. Pravdo, et al., "Seasat Synthetic Aperture Radar Data User's Manual," JPL publication 82-90, March 1, 1983;

[3] European Space Agency. ERS SAR RAW: ERS-1/2 synthetic aperture radar (SAR) annotated raw product data. http://earth1.esrin.esa.it:81/, 1998. Earthnet online.

[4] Yoshihisa Hara and Makoto Ono. Analysis of JERS-1 SAR imagery. In International Geoscience and Remote Sensing Symposium, Tokyo, Japan, 18-21 August 1993, pages 1191-1193, 1993

[5] M. Shimada, A. Rosenqvist, M. Watanabe, T. Tadono: “Polarimetric and interferometric potential of the PALSAR/ALOS”, in Proc. POLinSAR, 2005.

[6] Zebker and Villasenor, J. (1992). Decorrelation in interferometric radar echoes. IEEE Trans., 30, 950-959

[7] Massonnet D., Feigl K.L. (1998) Radar interferometry and its application to changes in the earth’s surface. Review of Geophysics, 36(4), 441-500.

[8] Rosen P., Hensley S., Joughin I., LI F., Madsen S., Rodriguesz E.,Goldstein R.(2000). Synthetic Aperture Radar Interferometry, Proc.IEEE March 2000, 333-379.

[9] Zebker H.A., Rosen P. (1997) Atmospheric Artifacts in Interferometric SAR surface deformation and topographic maps. J.Geophys.Res.-Solid Earth vol.102(B4), 7547-7563.

[10] Hansenn R. (2001). Radar Interferometry, Kluwer Academic Publishers

[11] P.Berardino, G.Fornaro, R.Lanari and E.Sansosti; “A new Algorithm for Surface Deformation Monitoring based on Small

Baseline Differential SAR Interferograms", IEEE Trans. Geosci. Remote Sens., 40, 11, 2002.

[12] Lanari R., Mora O., Manunta M., Mallorqui, J. J., Berardino P., Sansosti E. (2004) A Small Baseline Approach for Investigating Deformations on Full Resolution Differential SAR Interferograms. IEEE Transaction on Geoscience and Remote Sensing, 42, 7.

[13] Pepe, A. and Lanari, R. (2006) On the extension of the Minimum Cost Flow Algorithm for Phase Unwrapping of Multi-temporal Differential SAR Interferograms. IEEE Transactions on Geoscience and Remote Sensing, vol. 44, n.9, 2374-238.

[14] Goldstein R.M, (1995) Atmospheric limitations to repeat-track radar interferometry. Geophysical Research Letter, 22, pp.2517-2520

[15] Ferretti, A., Prati, C., and Rocca, F. (2000) Non-linear Subsidence Rate Estimation Using Permanent Scatterers in Differential SAR Interferometry. IEEE Transaction on Geoscience and Remote Sensing 38, 2202-2212.

[16] M. Manzo, G. P. Ricciardi, F. Casu, G. Ventura, G. Zeni, S. Borgström, P. Berardino, C. Del Gaudio, R. Lanari: Surface deformation analysis in the Ischia island (Italy) based on spaceborne radar interferometry, Journal of Volcanology and Geothermal Research, 151, pp 399-416, doi: 10.1016/j.jvolgeores.2005.09.010.

[17] Lundgren P., Casu F., Manzo M., Pepe A., Berardino P., Lanari R. (2004) Gravity and magma induced spreading of Mount Etna

[18] Cascini L., Ferlisi S., Fornaro G., Peduto D., Manunta M., Zeni G.(2007) Low and high resolution differential interferometry monitoring of the Sarno urban area. Rivista Italiana di Telerilevamento, 38, 23-33

[19] Perrone, A., Zeni, G., Piscitelli, S., Pepe, A., Loperte, A., Lapenna, V., Lanari, R. (2006) On the joint analysis of SAR Interferometry and Electrical Resistivity Tomography surveys for investigating ground deformations: the case-study of Satriano di Lucania (Potenza, Italy). Special issue of Engineering Geology on Remote sensing and ground-based geophysical techniques for recognition, characterization and monitoring of unstable slopes, 88, 260-273.

[20] Lanari, R., Casu, F., Manzo, M., Zeni, G., Berardino, P., Manunta, M., and Pepe, A. (2007), An overview of the Small Baseline Subset Algorithm: a DInSAR Technique for Surface Deformation

Analysis. Pure and Applied Geophysics (PAGEOPH), 164.4, 637-661, doi: 10.1007/S00024-007-0192-9

[21] Cascini L., Di Maio C. (1994) Emungimento delle acque sotterranee e cedimenti nell'abitato di Sarno: analisi preliminare. Rivista Italiana di Geotecnica, 3, 217-231

[22] Cascini L., Ferlisi S., Fornaro G., Lanari R., Peduto D., Zeni G. (2006) Subsidence monitoring in Sarno urban area via multitemporal DInSAR technique International Journal of Remote Sensing, 27(8), 1709-1716.

[23] M. Manunta, M. Marsella, G. Zeni, M. Sciotti, S. Atzori, R. Lanari, (2008) –Two-scale surface deformation analysis via the SBAS-DInSAR technique a case study of the city of Rome, Italy - International Journal of Remote Sensing- Vol 29 N.6 – pp.1665-1684

[24] Ventriglia U., and Sciotti M., 1970a, Geological Map of Roma. LAC., Firenze, Italy.

[25] Ventriglia U., and Sciotti M., 1970b, Thickness of the embankments, Geological Map of Roma, LAC., Firenze, Italy.

[26] Hsai-Yang Fang, 1990, Foundation Engineering Handbook, (Kluwer Academic Publishers Boston/Dordrecht/London)

[27] Funiciello R., Capelli G., Campolunghi M. P., Cecili A., and Mazza R., 2004, Geological-Technical Report, (in Italian),

http://www.urbanistica.comune.roma.it/giustinianoimperatore/a_ambito.html

[28] Cecchini D. EDS., 2005, Rifare Città, Cangemi, Roma, Italy (in Italian)

[29] Cardinali, M., Antonini, G., Reichenbach, P., and Guzzetti, F. (2001) Photo-geological and landslide inventory map for the Upper Tiber River basin. CNR, Gruppo Nazionale per la Difesa dalle Catastrofi Idrogeologiche, Publication n. 2154, scale 1:100,000.

[30] Servizio Geologico d'Italia (1980) Carta Geologica dell'Umbria. Map at 1:250,000 scale (in Italian).

[31] Guzzetti, F., Cardinali, M., and Reichenbach, P. (1996) The influence of structural setting and lithology on landslide type and pattern. Environmental and Engineering Geoscience 2:4, 531-555.

[32] Guzzetti, F., Ardizzone, F., Cardinali, M., Galli, M., and Reichenbach, P. (2008) Distribution of landslides in the upper Tiber River basin, central Italy. Geomorphology, Vol. 46, 1-2, 105-122.

[33] F. Guzzetti, M. Manunta, F. Ardizzone, A. Pepe, M. Cardinali, G. Zeni, P. Reichenbach ,R. Lanari -Analysis of ground deformation detected using the SBAS-DinSAR technique in Umbria, central Italy- accepted for publication in: Pure and Applied Geophysics, PAGEOPH

[34]Arpa(2007)
http://www.arpa.umbia.it/resource/docs/acquiferi_valle_umbra.pdf

[35] Berardino, P., Costantini, M. Franceschetti, G., Iodice, A., Pietranera, and L. Rizzo, V. (2003) Use of differential SAR interferometry in monitoring and modeling large slope instability at Maratea (Basilicata, Italy). Engin. Geol. 68: 31-51.

[36] Wasowski, J. and Singhroy, V. eds. (2003) Remote Sensing and Monitoring of landslides. Special Issue. Engineering Geology 68, 1-2.

[37] Hilley, G.E., Bürgmann, R., Ferretti, A., Novali, F., and Rocca, F. (2004) Dynamics of Slow-Moving Landslides from Permanent Scatterer Analysis. Science 304, 1952-1955.

[38] Colesanti, C. and Wasowski, J. (2006) Investigating landslides with space-borne Synthetic Aperture Radar (SAR) interferometry. Engineering Geology 88, 173-199.

[39] Canuti, P., Marcucci, E., Trastulli, S., Ventura, P., and Vincenti, G. (1986) Studi per la stabilizzazione della frana di Assisi. National Geotechnical Congress, Bologna, 14-16 May 1986, Vol. 1, 165-174.

[40] Felicioni, G., Martini, E. and Ribaldi, C. (1994) Studio dei Centri Abitati Instabili in Umbria. Rubettino Publisher, 418 p. (in Italian).

[41] Rum, G. (2003), COSMO-SkyMed: Mission definition and main applications and products, Proc. of POLinSAR 2003.

Acknowledgements

At the end of my PhD work, I feel indebted to many persons. First of all, I would like to sincerely thank Prof. Carmine Serio that gave to me the chance to attend the PhD course and for his constant encouragement. I am also extremely grateful to Dr. Riccardo Lanari for his continuous guidance throughout the course and his great patience in introducing me to the realm of Synthetic Aperture Radar.

A special thank goes to the research, technical and administrative staff of CNR-IREA for their support and for letting me at home in a friendly atmosphere.

Furthermore, I feel very obliged to Dr. Vincenzo Lapenna and Dr. Angela Perrone, from CNR-IMAA, for their valuable scientific cooperation. Finally, I want to acknowledge the scientific support received by Dr. Fausto Guzzetti and his team, from CNR-IRPI and Prof. Maria Marsella from University of Rome – La Sapienza.